



Numerical Simulation of An In-situ Fluid Injection Experiment into a Fault Using Coupled X-FEM Analysis

Adam K. Schwartzkopff¹ · Atsushi Sainoki¹ · Derek Elsworth²

Received: 1 April 2020 / Accepted: 31 October 2020
© Springer-Verlag GmbH Austria, part of Springer Nature 2020

Abstract

Fluid injection into a rock mass from industrial processes can cause perceivable seismic events that may raise public concern and affect the mechanical and physical properties of the rock mass. One such notable source of seismicity is from the additional fluid pressure added to the rock mass causing slip on faults. The aim is to provide a method to predict efficiently the fault mechanics due to anthropogenic fluid injection. This was achieved by extending a two-dimensional fully coupled fluid and mechanical loading extended finite element method (X-FEM) formulation via development of a standalone code in MATLAB. This code considers fluid flow along the fault as well as into the rock mass and uses a directly proportional equivalent injected flow rate into the fault as the input. This model was validated by comparing the resultant pressure, normal and tangential displacements at the center of the fault to a previously published in-situ experiment. The main results were that the mechanics of the fault could be simulated with sufficient accuracy using this approach given appropriate assumptions, measurements, and simplifications of the fault and rock properties. The main conclusion is that this coupled X-FEM approach may provide an efficient and accurate method to assist in predicting the fault mechanics due to fluid injection. These results are important, since it shows the applicability of X-FEM in predicting the mechanics of the fault and hence the applicability of this method to predict seismicity due to fluid injection.

Keywords Fault mechanics · Simulation · Coupled X-FEM · Induced seismicity

Abbreviations

DDM	Displacement discontinuity method
DEM	Distinct element method
DOF	Degrees of freedom
FEM	Finite element method
FLAC	Fast Lagrangian analysis of continua software
NoF	Number of fractures traversing the borehole section used for fluid injection
PEST	Parameter estimation software suite
SIMFIP	Step-rate injection method for fracture in-situ properties
TOUGH	A multiphase flow simulator

UDEC	Universal distinct element code
X-FEM	Extended finite element method

List of symbols

$2h$	Hydraulic aperture (m)
$2h_0$	Initial hydraulic aperture (m)
$2h_m$	Normal mechanical displacement (m)
$\bar{\mathbf{a}}_j(t)$	Enriched nodal DOF associated with the Heaviside function at node j
a	Empirical coefficient that controls the magnitude of the velocity frictional response
\mathbf{b}	Body force vector
b	Empirical coefficient that controls the magnitude of the hold time response
\mathbf{C}	Inertial matrix
$\bar{\mathbf{c}}_j(t)$	Enriched nodal DOF related to the modified level set function at node j
\mathbf{D}	Elastic tangential stiffness tensor
D_c	The slip required to renew contacts (m)
E	Elastic modulus (Pa)
\bar{E}	Effective elastic modulus in the direction normal to the discontinuity (Pa)
$\mathbf{f}_U^{\text{ext}}$	External force vector

✉ Adam K. Schwartzkopff
aschwartzkopff@kumamoto-u.ac.jp

¹ International Research Organization for Advanced Science and Technology, Kumamoto University, Kumamoto, Kumamoto Prefecture 860-8555, Japan

² Department of Energy and Mineral Engineering, G3 Centre and Energy Institute, The Pennsylvania State University, University park, PA 16802, USA

$\mathbf{f}_\alpha^{\text{int}}$	Internal contact force vector
\overline{G}	Shear modulus (Pa)
\overline{G}	Effective tangential shear modulus (Pa)
\mathbf{g}_T	Tangential displacement (m)
\mathbf{g}_N	Normal displacement (m)
\mathbf{H}	Permeability matrix
H	Heaviside enrichment function
\mathbf{J}	Jacobian matrix
\mathbf{K}	Stiffness matrix
K_f	Fluid bulk modulus (Pa)
K_s	Solid bulk modulus (Pa)
k_f	Permeability matrix ($\text{m}^3 \cdot \text{s} / \text{kg}$)
k_{f_d}	Fault permeability ($\text{m}^3 \cdot \text{s} / \text{kg}$)
\overline{k}_d	Single discontinuity normal stiffness (Pa/m)
\overline{k}_N	Apparent normal stiffness (Pa/m)
\overline{k}_T	Single discontinuity tangential stiffness (Pa/m)
\overline{k}_T	Apparent tangential stiffness (Pa/m)
L_N^d	Normal effective discontinuity length to calculate the apparent normal stiffness (m)
L_T^d	Tangential effective discontinuity length to calculate the apparent tangential stiffness (m)
N	Standard shape functions
\mathbf{N}^{std}	Standard shape function matrix over the discontinuity
\mathbf{n}_{Γ_d}	Fault unit normal vector
n	Porosity
\overline{P}	Standard and enriched DOF of pressure
$\mathbf{p}(x, t)$	Enriched pore pressure field (Pa)
$\overline{\mathbf{p}}_i(t)$	Standard nodal pressure at node i (Pa)
p	Pore pressure (Pa)
p_0	Initial pore pressure (Pa)
\mathbf{p}_N	Normal traction (Pa)
\mathbf{p}_T	Tangential traction (Pa)
\mathbf{Q}	Coupling matrix
$\mathbf{q}_p^{\text{ext}}$	External flux vector
$\mathbf{q}_p^{\text{int}}$	Internal flux vectors
q	Injected flow rate into fault (m/s)
\overline{q}	Flux vector at boundary
\mathbf{S}	Compressibility matrix
S	Discontinuity spacing (m)
$\overline{\mathbf{t}}$	Tractions on boundary
\mathbf{t}_{Γ_d}	Fault unit tangential vector
t	Time (s)
$\mathbf{u}(x, t)$	Enriched displacement field (m)
$\overline{\mathbf{u}}_i(t)$	Standard nodal displacements at node i (m)
$\dot{\mathbf{u}}$	Velocity vector (m/s)
$\ddot{\mathbf{u}}$	Acceleration vector (m / s^2)
\overline{U}	Standard and enriched DOF of displacement
V	Tangential velocity at a point along the fault (m/s)
V_0	Reference tangential velocity (m/s)

Greek letters

α_{Biot}	Biot poroelastic constant
θ	Contact time parameter
κ	Factor to account for the deviation from parallel fault surfaces
μ	Friction coefficient
μ_0	Residual friction coefficient
μ_{f_d}	Dynamic viscosity of the fluid (Pa.s)
ν	Poisson's ratio
$\overline{\nu}$	Effective Poisson's ratio for the discontinuity system
ρ	Average density (kg / m^3)
ρ_f	Fluid density (kg / m^3)
ρ_s	Solid density (kg / m^3)
$\boldsymbol{\sigma}$	Total stress tensor (Pa)
$\boldsymbol{\sigma}_0$	In-situ effective stress tensor (Pa)
σ_h	Standard deviation of non-logrithmized fracture asperity heights (m)
σ'_n	Effective normal compressive stress (Pa)
τ	Shear stress at point along fault (Pa)
$\varphi(x)$	Normal level set function
φ_d	Dilation angle ($^\circ$)
$\psi(x)$	Modified level set function

1 Introduction

Fluid injection into or near a fault may induce slip and result in seismicity of sufficient magnitude to cause damage to surface structures (Raleigh et al. 1976; Nicholson and Wesson 1992; Cornet et al. 1997; Majer et al. 2007; Ellsworth 2013). Such activities include hydraulic fracturing and wastewater disposal in the context of geothermal energy, unconventional hydrocarbon production, and destressing in deep hard rock mines. Understanding the mechanics of fault reactivation is, therefore, important in calculating the anticipated seismicity in geological formations. Understanding the response to fluid-injection is particularly difficult due to the innately coupled nature of the fluid-transmission and mechanical processes. Previous studies have mainly focused on developing numerical tools (Rutqvist et al. 2002) to generate parametric results (Rutqvist et al. 2013, 2015). It is important, however, to validate these approaches using observations at appropriate length- and time-scales of interest. The potential for rupture is intrinsically related to rates of injection relative to permeability of the host—as this controls the rate of pressurization in driving failure and the rate of depressurization in mitigating failure. To represent accurately fault mechanics driven by fluid injection, a few key characteristics should be considered. That is, that:

- (i) the true nature of the coupling between fluid and mechanical process is captured, including fluid flow within the fault as well as leak-off into the rock mass,
- (ii) appropriate rock properties can be determined and input into the model,
- (iii) the method is sufficiently efficient to be useful in an industrial context, and
- (iv) results are comparable to in-situ experiments.

Thus, the problem addressed in this study is reproducing the mechanics of a natural in-situ fault using a coupled extended finite element method (X-FEM) approach, using the flow rates from the experiment as the input.

Fault slip driven-by fluid injection is broadly explained by the Coulomb friction law (Raleigh et al. 1976; Streit and Hillis 2004; Rutqvist et al. 2007; Moeck et al. 2009; Cuss and Harrington 2016; Wiseall et al. 2018). An increase in pore pressure decreases the compressive effective normal stress along the fault that also decreases the frictional resistance. The remnant shear stress within the fluid-pressurized region with reduced normal effective stress then drives shear failure. A simplified approach to determining whether the fault will slip due to a certain amount of localized fluid pressure is termed slip tendency analysis (Streit and Hillis 2004; Moeck et al. 2009). The pore pressure is increased “virtually” until the ratio of the shear stress along the fault plane to the compressive effective normal stress is equal to or slightly greater than the assumed frictional coefficient. This method allows the straightforward determination of the fluid pressure required to reactivate the fault and cause slip at a certain location. The resulting “virtual” fault movement is, however, more difficult to predict, since this is dependent on the distribution of fluid pressures along the fault and into the rock mass, the rock and fault properties and the in-situ effective stress regime.

Laboratory studies indicate that Coulomb friction is valid as a first approximation to predict the onset of fault reactivation due to fluid injection. However, the processes governing fault reactivation are complex, especially when considering gas injection, but this is beyond the scope of the work presented here (Cuss and Harrington 2016; Wiseall et al. 2018). The complex nonlinear behavior of fault slip can be readily described by rate and state friction laws (Dieterich 1979; Ruina 1983), where frictional coefficient is dependent on both the velocity of slip and evolves with time (Marone 1998). Such laboratory studies indicate that the slip magnitude at the center of an injection section could possibly be predicted when using an appropriate modelling technique. This slip may be either seismic or aseismic.

Seismic slip occurs when the failure of the fault is unstable; that is, when the resistance to sliding decreases more rapidly than the unloading process—represented by a loading system that is softer than fault. Conversely, aseismic

slip occurs when the fault is softer than the loading system (Guglielmi et al. 2015a). In natural and artificially perturbed fault systems, slip may occur both seismically and aseismically. Seismic slip of sufficiently large energy release may pose a safety risk to structures and people (Scotti and Cornet 1994; Cornet et al. 1997; Guglielmi et al. 2015a), where the maximum energy release (logarithmically scaled to Richter magnitude) could be dependent on the volume or rate of fluid injection (McGarr 2014).

Extended finite element (X-FEM) modelling was originally developed to represent fracture propagation (Mohammadnejad and Khoei 2013; Khoei et al. 2018) and may be readily applied to represent the nonlinear shear behavior of discontinuous rock due to fluid injection (Pan et al. 2013). The present study extends a coupled two-dimensional X-FEM formulation (Khoei 2014) to the mechanics of fluid injection into an in-situ natural fault. This approach was validated against a highly constrained in-situ fault reactivation experiment (Guglielmi et al. 2015a), where tangential and normal displacement of the fault were recorded with the progress of fluid injection. This validated approach accommodates all essential features of the reactivation (viz. fluid injection, leak-off, and stiffness contrasts in the system). This method may be used to represent the mechanical behavior of other faults perturbed by fluid injection. Such analyses may be applied to discriminate between stable and unstable reactivation of faults and to mitigate the impacts of seismicity.

2 X-FEM Formulation

X-FEM modeling was selected, as it is particularly computationally efficient when accommodating multiple discontinuities. In comparison to traditional finite element methods (FEM), X-FEM methods implicitly represent individual cracks without requiring complex meshing and remeshing of the feature—resulting in decreased computation time. Specifically, the X-FEM approach enriches the FEM model by providing additional degrees of freedom (DOF) to the nodes of the element(s) that are intersected by the discontinuity. Therefore, a single mesh can be used for discontinuities of any length and orientation (Giner et al. 2009). The main disadvantage to the X-FEM is the potential numerical instabilities caused by an ill-conditioned stiffness matrix. This can be caused by the discontinuity being too close to the element edges. In the simulations produced in this study, the discontinuity geometry was simple with respect to the mesh and a preconditioning scheme was implemented (Béchet et al. 2005) which assisted in producing a stable converged solution.

The following sections introduce the X-FEM method used (Khoei 2014) and the model parameters used to simulate the in-situ experiment (Guglielmi et al. 2015a).

2.1 General Assumptions for Determination of the Governing and Constitutive Equations

A modified version of the X-FEM (Khoei 2014) code was used, incorporating reasonable assumptions:

- The coupled movements are sub-inertial:
Seismic (inertial) stress waves cannot be captured using this approach. However, since most of the fault slip occurred aseismically/sub-seismically in the experiment, and we are principally interested in triggering, this can be considered an adequate approximation.
- Flow is laminar within the fracture:
Turbulent flow would only occur if the flow rates were extremely high. In the in-situ experiment, the maximum flow rate was ~61 l per minute, anticipated to produce only laminar flow within the fault.
- The rock mass is fully saturated before injection:
The in-situ experiment was 282 m underground and below the water table.

2.2 Governing Equations for Deformable Porous Media

A porous medium comprises a solid granular skeleton containing at least one fluid phase within the voids (or pores). The *linear momentum balance of the solid and fluid mixture* can be expressed as follows, neglecting the relative acceleration of the fluid phase with respect to the solid phase (Khoei 2014):

$$\nabla \cdot \boldsymbol{\sigma} - \rho \ddot{\mathbf{u}} + \rho \mathbf{b} = 0, \quad (1)$$

where $\boldsymbol{\sigma}$ is the total stress tensor, $\ddot{\mathbf{u}}$ is the acceleration vector of the solid phase, \mathbf{b} is the body force vector, ρ is the average density of the mixture and the ∇ symbol is the vector gradient operator. The density of the rock medium is defined as $\rho = n\rho_f + (1 - n)\rho_s$, where n is the porosity, ρ_f is the density of the fluid that fills the voids (or pores) and ρ_s is the density of the solid grains.

Conservation of linear momentum for the fluid flow combined with *continuity of the fluid phase* results in the following governing equation for the fluid (Khoei 2014):

$$\nabla \cdot [\mathbf{k}_f(-\nabla p - \rho_f \ddot{\mathbf{u}} + \rho_f \mathbf{b})] + \alpha_{\text{Biot}} \nabla \cdot \dot{\mathbf{u}} + \frac{1}{Q} \dot{p} = q, \quad (2)$$

where \mathbf{k}_f is the permeability matrix of the porous medium, p is the pore pressure, ρ_f is the density of the fluid, α_{Biot} is the Biot poroelastic constant (Biot 1941), $\dot{\mathbf{u}}$ is the velocity of the mixture, \dot{p} is the gradient of the pore pressure and q is the external flow or injected fluid. In addition, $1/Q = (\alpha_{\text{Biot}} - n)/K_s + n/K_f$, where K_s and K_f are the bulk

moduli of the solid and fluid phases, respectively. Note that the permeability matrix of this work comprises permeability magnitudes divided by the dynamic viscosity (Prévost and Sukumar 2016).

These governing equations (Eq. 1 and Eq. 2) can be solved for a fractured porous medium as presented below.

2.3 Approximate Displacement and Pressure Fields

In X-FEM, the shape functions normally used by the FEM are enriched using appropriate functions based on the type of embedded discontinuity. The hydro-mechanical coupling process is hence captured using suitable enrichment functions to describe the tractions on the fault face, fluid leak-off from the fault into the porous medium and fluid pressure and displacement fields. The displacement field is assumed to be discontinuous over the fault face, and the fluid pressure field is assumed to be continuous. However, its gradient normal to the fault is discontinuous over that fault face. The Heaviside function is used to capture this displacement discontinuity over the fault face, and the modified level set function is utilized to model the fluid pressure field, which represents the discontinuous gradient normal to the fault face (Khoei 2014).

The enriched displacement field $\mathbf{u}(x, t)$ can be expressed as

$$\mathbf{u}(x, t) = \sum_{i=1}^N N_i(x) \bar{\mathbf{u}}_i(t) + \sum_{j=1}^M N_j(x) (H(\varphi(x)) - H(\varphi(x_j))) \bar{\mathbf{a}}_j(t), \quad (3)$$

where x is the location of the point of interest, t is the time step, N represents the standard shape functions, N is the number of all nodal points, and M is the number of enriched nodes that are bisected by the fault. In Eq. 3 $\bar{\mathbf{u}}_i(t)$ are the unknown standard nodal displacements at node i and $\bar{\mathbf{a}}_j(t)$ are the unknown enriched nodal DOF associated with the Heaviside function at node j .

The discontinuous (Heaviside) enrichment function $H(\varphi(x))$ is defined using the step enrichment function:

$$\psi_{\text{step}}(\varphi(x)) = H(\varphi(x)) = \begin{cases} 0 & \text{if } \varphi(x) \leq 0 \\ 1 & \text{if } \varphi(x) > 0 \end{cases}, \quad (4)$$

where $\varphi(x)$ is the normal-level set function; along the strong discontinuity (that is the fault), and its value is zero. If the point is below or to the left of the fault, the level set function is negative; and, if the point is above or to the right of the fault, the level set function is positive. This is with respect to the global coordinate system of the model (see Fig. 1 and Eq. 5):

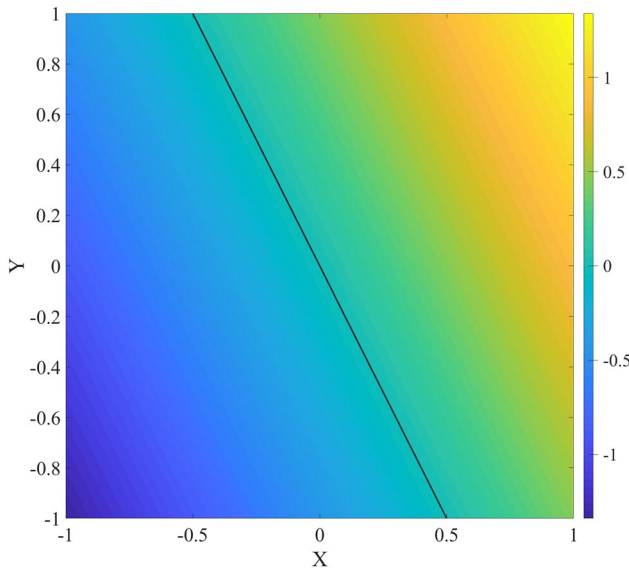


Fig. 1 Level set function example (the black line represents the strong discontinuity)

$$\varphi(x) = \frac{(x_2 - x_1)(y_1 - y_0) - (x_1 - x_0)(y_2 - y_1)}{\sqrt{(x_2 - x_1)^2 + (y_2 - y_1)^2}}, \quad (5)$$

where (x_1, y_1) and (x_2, y_2) are two points on the line and $x = (x_0, y_0)$ is the point of interest.

The enriched approximation of the X-FEM pressure field $\mathbf{p}(x, t)$ is defined as

$$\mathbf{p}(x, t) = \sum_{i=1}^N N_{P_i}(x) \bar{\mathbf{p}}_i(t) + \sum_{j=1}^M N_{P_j}(x) (\psi(x) - \psi(x_j)) \bar{\mathbf{c}}_j(t), \quad (6)$$

where $\bar{\mathbf{p}}_i(t)$ is the unknown standard nodal pressure at node i and $\bar{\mathbf{c}}_j(t)$ are the unknown enriched nodal DOF related to the modified level set function at node j . In Eq. 6 $N_{P_i}(x)$ represent the standard shape functions and $\psi(x)$ is the modified level set function, which can be defined as

$$\psi(x) = \sum_i^M N_{P_i}(x) |\varphi_i| - \left| \sum_i^M N_{P_i}(x) \varphi_i \right|, \quad (7)$$

where φ_i are the nodal values of the level set function. The normal gradient of this function is discontinuous across the face of the fault, which captures leak-off from the fault.

2.4 Spatial Discretization of the Strong Formulae for X-FEM

The weak forms of the aforementioned governing equations are obtained by applying the well-known divergence

theorem, which are then, discretized spatially using Eqs. 3 and 6, based on the Galerkin discretization technique. Then, the following system of linear equations results:

$$\begin{aligned} \mathbf{K} \bar{\mathbf{U}} - \mathbf{Q} \bar{\mathbf{P}} + \mathbf{f}_U^{\text{int}} - \mathbf{f}_U^{\text{ext}} &= \mathbf{0} \\ \mathbf{C} \ddot{\bar{\mathbf{U}}} + \mathbf{Q}^T \dot{\bar{\mathbf{U}}} + \mathbf{H} \bar{\mathbf{P}} + \mathbf{S} \dot{\bar{\mathbf{P}}} - \mathbf{q}_p^{\text{int}} - \mathbf{q}_p^{\text{ext}} &= \mathbf{0}, \end{aligned} \quad (8)$$

where $\bar{\mathbf{U}} = \langle \bar{\mathbf{u}}, \bar{\mathbf{a}} \rangle$ and $\bar{\mathbf{P}} = \langle \bar{\mathbf{p}}, \bar{\mathbf{c}} \rangle$ are standard and enriched DOF of displacement and pressure, respectively. \mathbf{K} is the stiffness matrix, \mathbf{Q} is the coupling matrix, \mathbf{H} is the permeability matrix, \mathbf{S} is the compressibility matrix, \mathbf{C} is the inertial matrix, and $\mathbf{f}_U^{\text{ext}}$ and $\mathbf{q}_p^{\text{ext}}$ are the external force vectors as defined by

$$\mathbf{K}_{\alpha\beta} = \int_{\Omega} (\mathbf{B}_u^\alpha)^T \mathbf{D} \mathbf{B}_u^\beta d\Omega$$

$$\mathbf{Q}_{\alpha\gamma} = \int_{\Omega} (\mathbf{B}_u^\alpha)^T \alpha_{\text{Biot}} \mathbf{m} \mathbf{N}_p^\beta d\Omega$$

$$\mathbf{f}_\alpha^{\text{ext}} = \int_{\Omega} (\mathbf{N}_u^\alpha)^T \rho \mathbf{b} d\Omega + \int_{\Gamma_t} (\mathbf{N}_u^\alpha)^T \bar{\mathbf{t}} d\Gamma - \int_{\Omega} (\mathbf{B}_u^\alpha) \sigma_0 d\Omega$$

$$\mathbf{C}_{\delta\beta} = \int_{\Omega} (\nabla \mathbf{N}_p^\delta)^T k_f \rho_f \mathbf{N}_p^\beta d\Omega$$

$$\mathbf{H}_{\delta\gamma} = \int_{\Omega} (\nabla \mathbf{N}_p^\delta)^T k_f (\nabla \mathbf{N}_p^\gamma) d\Omega$$

$$\mathbf{S}_{\delta\gamma} = \int_{\Omega} (\mathbf{N}_p^\delta)^T \frac{1}{Q} \mathbf{N}_p^\gamma d\Omega$$

$$\mathbf{q}_\delta^{\text{ext}} = \int_{\Omega} (\nabla \mathbf{N}_p^\delta) k_f \rho_f \mathbf{b} d\Omega - \int_{\Gamma_w} (\mathbf{N}_p^\delta)^T \bar{q} d\Gamma,$$

where $(\alpha, \beta) \in (\text{std}, \text{Hev})$ represent the standard and Heaviside functions of the displacement field and $(\delta, \gamma) \in (\text{std}, \text{abs})$ are the standard and modified level set functions of the pressure field. In these above definitions: \mathbf{D} is the elastic tangential stiffness tensor; $\mathbf{m} = \{ 1 \ 1 \ 0 \}^T$ and the fluid flow at the boundary is signified as \bar{q} . In addition, $\bar{\mathbf{t}}$ denotes the tractions on the boundary and the in-situ effective stress matrix is denoted σ_0 , which varies with depth. The influence of in-situ effective stress is automatically incorporated into the formulation.

In addition, the flux vectors $\mathbf{q}_p^{\text{int}}$ that account for fluid exchange between the fault and the surrounding porous rock, can be defined as (Khoei 2014):

$$\begin{aligned}
 \mathbf{q}_\delta^{\text{int}} = & - \int_{\Gamma_d} (\nabla N_p^\delta)^T \mathbf{t}_{\Gamma_d} k_{f_d}(2h) \nabla p \mathbf{t}_{\Gamma_d} d\Gamma - \int_{\Gamma_d} (\nabla N_p^\delta)^T \mathbf{t}_{\Gamma_d} k_{f_d} \rho_f(2h) \langle \dot{\mathbf{u}} \rangle \mathbf{t}_{\Gamma_d} d\Gamma \\
 & - \int_{\Gamma_d} (N_p^\delta)^T \alpha_{\text{Biot}}(2h) \mathbf{t}_{\Gamma_d} \langle \nabla \dot{\mathbf{u}} \rangle \mathbf{t}_{\Gamma_d} d\Gamma - \int_{\Gamma_d} (N_p^\delta)^T \alpha_{\text{Biot}} [[\dot{\mathbf{u}}]] \mathbf{n}_{\Gamma_d} d\Gamma \\
 & - \int_{\Gamma_d} (N_p^\delta)^T (2h) \frac{1}{K_f} \dot{p} d\Gamma + \int_{\Gamma_d} (\nabla N_p^\delta)^T \mathbf{t}_{\Gamma_d} k_{f_d} \rho_f(2h) \mathbf{b} \mathbf{t}_{\Gamma_d} d\Gamma + \int_{\Gamma_d} (N_p^\delta)^T (2h) q d\Gamma,
 \end{aligned} \tag{10}$$

where \mathbf{t}_{Γ_d} and \mathbf{n}_{Γ_d} are the unit tangent and unit normal vectors to the fault, q is the injected flow rate into the fault and $2h$ is the average small distance between the two fault faces, due to the roughness of the fault and is equivalent to the hydraulic aperture. The last term in Eq. 10 has been added to the formulation to allow for fluid injection (or extraction) from the model along the fault. The intrinsic permeability of the fault k_{f_d} may be determined from the cubic law. The cubic law was multiplied by $1/\kappa$, where the kappa κ value ranges from 1 to 1.65 and accounts for the deviation of the fault faces from parallel (Khoei 2014).

2.5 Discretization of the Time Domain and Solution Technique

By utilizing the Newmark–Beta scheme for the time discretization of the unknown variables, the following non-linear set of equations result:

$$\begin{aligned}
 \Psi_{U_{n+1}} &= \mathbf{K} \bar{U}_{n+1} - \mathbf{Q} \bar{P}_{n+1} + \mathbf{f}_{U_{n+1}}^{\text{int}} - \mathbf{f}_{U_{n+1}}^{\text{ext}} = \mathbf{0} \\
 \Psi_{P_{n+1}} &= \frac{1}{\beta \Delta t^2} \mathbf{C} \bar{U}_{n+1} + \frac{\gamma}{\beta \Delta t} \mathbf{Q}^T \bar{U}_{n+1} + \mathbf{H} \bar{P}_{n+1} + \frac{1}{\theta \Delta t} \mathbf{S} \bar{P}_{n+1} - \mathbf{q}_P^{\text{int}} - \mathbf{G}_{P_{n+1}} = \mathbf{0},
 \end{aligned} \tag{11}$$

where $\mathbf{G}_{P_{n+1}}$ is the vector of known values at time t_n and are defined as

$$\begin{aligned}
 \mathbf{G}_{P_{n+1}} = & \mathbf{q}_{P_{n+1}}^{\text{ext}} + \mathbf{C} \left(\frac{1}{\beta \Delta t^2} \bar{U}_n - \frac{1}{\beta \Delta t} \dot{\bar{U}}_n - \left(\frac{1}{2\beta} - 1 \right) \ddot{\bar{U}}_n \right) \\
 & + \mathbf{Q}^T \left(\frac{\gamma}{\beta \Delta t} \bar{U}_n - \left(\frac{\gamma}{\beta} - 1 \right) \dot{\bar{U}}_n - \Delta t \left(\frac{\gamma}{2\beta} - 1 \right) \ddot{\bar{U}}_n \right) + \mathbf{S} \left(\frac{1}{\theta \Delta t} \bar{P}_n - \left(\frac{1}{\theta} - 1 \right) \dot{\bar{P}}_n \right).
 \end{aligned} \tag{12}$$

This non-linear system of equations is solved by Newton–Raphson iteration, where the relative error for each time step in the simulations is set to $< 1\%$. The linear approximation is defined as

$$\begin{Bmatrix} \Psi_{U_{n+1}}^{i+1} \\ \Psi_{P_{n+1}}^{i+1} \end{Bmatrix} = \begin{Bmatrix} \Psi_{U_{n+1}}^i \\ \Psi_{P_{n+1}}^i \end{Bmatrix} + \mathbf{J} \begin{Bmatrix} dU_n^i \\ dP_n^i \end{Bmatrix} = \mathbf{0}, \tag{13}$$

where the Jacobian matrix is

$$\mathbf{J} = \begin{bmatrix} \mathbf{K} + \frac{\partial \mathbf{f}_U^{\text{int}}}{\partial U} & -\mathbf{Q} + \frac{\partial \mathbf{f}_U^{\text{int}}}{\partial P} \\ \frac{1}{\beta \Delta t^2} \mathbf{C} + \frac{\gamma}{\beta \Delta t} \mathbf{Q}^T - \frac{\partial \mathbf{q}_P^{\text{int}}}{\partial U} & \mathbf{H} + \frac{1}{\theta \Delta t} \mathbf{S} - \frac{\partial \mathbf{q}_P^{\text{int}}}{\partial P} \end{bmatrix}. \tag{14}$$

To reduce the computational cost, the Jacobian matrix is made symmetrical by multiplying the first row by $-\gamma/\beta \Delta t$ and the inertial matrix \mathbf{C} , is removed, since this exerts little influence on the dynamic seepage terms. Note that this means that the \mathbf{C} term is removed from Eqs. 11 and 12. In addition, it can be shown that $\partial \mathbf{f}_U^{\text{int}}/\partial U$ is zero. It is assumed that $\partial \mathbf{f}_U^{\text{int}}/\partial P = (\beta \Delta t/\gamma)(\partial \mathbf{q}_P^{\text{int}}/\partial U)$ to ensure that the Jacobian is symmetric. The term $\partial \mathbf{f}_U^{\text{int}}/\partial P$ is

$$\frac{\partial \mathbf{f}_U^{\text{int}}}{\partial P} = - \int_{\Gamma_d} [[N_u^\alpha]]^T \mathbf{n}_{\Gamma_d} N_p^\delta d\Gamma. \tag{15}$$

In addition, $\partial \mathbf{q}_P^{\text{int}}/\partial P$ is defined as

$$\begin{aligned}
 \frac{\partial \mathbf{q}_P^{\text{int}}}{\partial P} = & - \int_{\Gamma_d} (\nabla N_p^\delta)^T \mathbf{t}_{\Gamma_d} k_{f_d}(2h) \mathbf{t}_{\Gamma_d}^T \nabla N_p^\gamma d\Gamma \\
 & - \frac{1}{\theta \Delta t} \int_{\Gamma_d} (N_p^\delta)^T (2h) \frac{1}{K_f} N_p^\gamma d\Gamma
 \end{aligned} \tag{16}$$

defining the full suite of terms contributing to the Jacobian.

2.6 Frictional Model

A modified version of the Coulomb friction law using a rate parameter is implemented in the X-FEM model (Dieterich 1979). For cohesionless frictional faults, the original Coulomb friction law can be expressed simply as

$$|\tau| = \mu \sigma'_n, \tag{17}$$

where τ is the shear stress that is present at a location along the fault, σ'_n is the effective normal compressive stress and μ is the friction coefficient. The frictional coefficient can vary over the length of the fault. The effective normal compressive stress is simply the normal compressive stress minus the fluid pressure along the fault—assuming a Biot coefficient α_{Biot} of unity. Note that if the effective normal compressive stress becomes tensile, when the fluid pressure is greater than the normal compressive stress, the shear stress and strength reduce to zero and this point along the fault must slip, since this discontinuity is then considered open. This friction law hence determines under what stress conditions a fault surface will slip. Rate state friction relates the friction coefficient to the rate of tangential shear displacement and the duration at that state (Marone 1998). The Dieterich constitutive law, which is used to simulate dynamic frictional response, can be expressed as

$$\mu = \mu_0 + a \ln \left(\frac{V}{V_0} \right) + b \ln \left(\frac{V_0 \theta}{D_c} \right) \text{ and } \frac{d\theta}{dt} = 1 - \frac{V\theta}{D_c}, \tag{18}$$

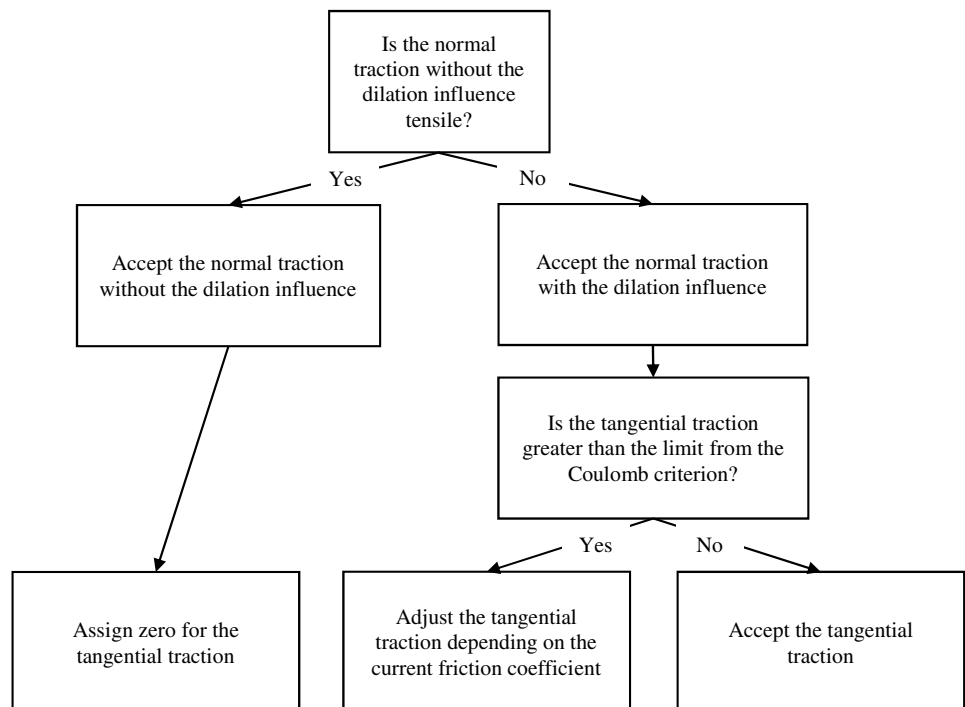
where μ_0 is the residual frictional coefficient, a is an empirical dimensionless coefficient which controls the magnitude of the velocity response, V is the tangential velocity, and V_0 is a reference velocity. The parameter b is an empirical dimensionless coefficient that controls the state response, D_c has been interpreted as the slip required to renew surface contacts and θ is the contact time parameter. This constitutive law provides a relationship that captures the time and velocity dependence of friction.

2.7 Contact Model

The presence of a fault and the application of effective compressive stresses on that discontinuity result in contact and closure. Thus, a contact model must be used in the simulations. In this work, a penalty method is used to model the contact constraint. This method allows for only slight interpenetration between two contacting surfaces. A normal contact force is associated with this slight overlap and is determined using the normal stiffness of the contact interface and the observed interpenetration. To utilize contact conditions the following integration functions are used to calculate the internal enriched force terms in Eq. 8 (that is, for $\mathbf{f}_U^{\text{int}}$):

$$\mathbf{f}_\alpha^{\text{int}} = \int_{\Gamma_c} (\mathbf{N}^{\text{std}})^T \left[\bar{k}_N (\mathbf{n}_{\Gamma_d} \otimes \mathbf{n}_{\Gamma_d}) + \bar{k}_T (\mathbf{I} - \mathbf{n}_{\Gamma_d} \otimes \mathbf{n}_{\Gamma_d}) \right] \bar{\mathbf{a}} d\Gamma - \int_{\Gamma_c} (\mathbf{N}^{\text{std}})^T p \mathbf{n}_{\Gamma_d} d\Gamma, \tag{19}$$

Fig. 2 Frictional contact flow chart



where \mathbf{N}^{std} is the standard shape function matrix over the discontinuity, $\left[\bar{k}_N(\mathbf{n}_{\Gamma_d} \otimes \mathbf{n}_{\Gamma_d}) + \bar{k}_T(\mathbf{I} - \mathbf{n}_{\Gamma_d} \otimes \mathbf{n}_{\Gamma_d})\right]\bar{\mathbf{a}}$ is the contact traction and p is the change in pore pressure. \bar{k}_N is the apparent normal stiffness and \bar{k}_T is the apparent tangential stiffness of the fault. Note the contact traction is modified according to the predictor–corrector algorithm (see Fig. 2 and method below).

In addition, the stiffness matrix \mathbf{K} must be modified when there is contact to the following:

$$\mathbf{K} = \begin{bmatrix} \int_{\Omega} (\mathbf{B}^{\text{std}})^T \mathbf{D} \mathbf{B}^{\text{std}} d\Omega & \int_{\Omega} (\mathbf{B}^{\text{std}})^T \mathbf{D} \mathbf{B}^{\text{enr}} d\Omega \\ \int_{\Omega} (\mathbf{B}^{\text{enr}})^T \mathbf{D} \mathbf{B}^{\text{enr}} d\Omega & \\ \int_{\Omega} (\mathbf{B}^{\text{enr}})^T \mathbf{D} \mathbf{B}^{\text{std}} d\Omega & \\ + \int_{\Gamma_c} (\mathbf{N}^{\text{std}}) \left[\bar{k}_N(\mathbf{n}_{\Gamma_d} \otimes \mathbf{n}_{\Gamma_d}) + \bar{k}_T(\mathbf{I} - \mathbf{n}_{\Gamma_d} \otimes \mathbf{n}_{\Gamma_d})\right] \mathbf{N}^{\text{std}} d\Gamma & \end{bmatrix}, \tag{20}$$

where $\int_{\Gamma_c} (\mathbf{N}^{\text{std}}) \left[\bar{k}_N(\mathbf{n}_{\Gamma_d} \otimes \mathbf{n}_{\Gamma_d}) + \bar{k}_T(\mathbf{I} - \mathbf{n}_{\Gamma_d} \otimes \mathbf{n}_{\Gamma_d})\right] \mathbf{N}^{\text{std}} d\Gamma$ is the contact stiffness matrix and $\mathbf{f}_{\alpha}^{\text{int}}$ can be taken as the contact force vector.

The following modified predictor–corrector algorithm is used for the frictional contact problem (see Fig. 2 for the flow chart of this method):

The normal traction is evaluated:

$$\mathbf{p}_{N_{n+1}}^{i+1} = \mathbf{p}_{N_{n+1}}^{i+1} + \left[\bar{k}_N(\mathbf{n}_{\Gamma_d} \otimes \mathbf{n}_{\Gamma_d})\right] \Delta \mathbf{g}_{N_{n+1}}^{i+1} \cdot \mathbf{n}_{\Gamma_d} - \bar{k}_N \left|\Delta \mathbf{g}_{T_{n+1}}^{i+1}\right| \tan(\varphi_d) \tag{21}$$

with the influence of dilation angle added to the formulation, where φ_d is the dilation angle with compression defined as negative. The symbols i and n indicate the time step and Newton–Raphson iteration, respectively.

1. The elastic predictor phase is calculated:

$$\left(\mathbf{p}_{T_{n+1}}^{i+1}\right)^{\text{trial}} = \mathbf{p}_{T_{n+1}}^{i+1} + \left[\bar{k}_T(\mathbf{I} - \mathbf{n}_{\Gamma_d} \otimes \mathbf{n}_{\Gamma_d})\right] \Delta \mathbf{g}_{T_{n+1}}^{i+1} \cdot \mathbf{t}_{\Gamma_d}. \tag{22}$$

2. The elastic frictional traction trial value is calculated, and the current stick–slip condition is checked:

If

$$\mathbf{p}_{N_{n+1}}^{i+1} + \left[\bar{k}_N(\mathbf{n}_{\Gamma_d} \otimes \mathbf{n}_{\Gamma_d})\right] \Delta \mathbf{g}_{N_{n+1}}^{i+1} \cdot \mathbf{n}_{\Gamma_d} \geq 0. \tag{23}$$

Then accept the normal traction and assign zero for the tangential force:

Else if

$$F_f = \left\| \left(\mathbf{p}_{T_{n+1}}^{i+1}\right)^{\text{trial}} \right\| - \mu \left\| \mathbf{p}_{N_{n+1}}^{i+1} \right\| < 0. \tag{24}$$

Then accept the tangential force as the final value.

Else the plastic (slip) corrector phase is used, whereby the trial value of frictional traction is recalculated as

$$\mathbf{p}_{T_{n+1}}^{i+1} = \mu \left\| \mathbf{p}_{N_{n+1}}^{i+1} \right\| \frac{\Delta \mathbf{g}_{T_{n+1}}^{i+1}}{\left\| \Delta \mathbf{g}_{T_{n+1}}^{i+1} \right\|}. \tag{25}$$

The tangential displacement increment $\Delta \mathbf{g}_{T_{n+1}}^{i+1}$ can be calculated as follows:

$$\Delta \mathbf{g}_{T_{n+1}}^{i+1} \equiv -\mathbf{N}^{\text{std}} \Delta \bar{\mathbf{a}} \cdot \mathbf{t}_{\Gamma_d}, \tag{26}$$

where $\Delta \bar{\mathbf{a}}$ is the change in the vector $\bar{\mathbf{a}}$ —from the previously converged value $\bar{\mathbf{a}}_{n=1}^{i+1}$ to the updated $\bar{\mathbf{a}}_{n+1}^{i+1}$. The change $\Delta \bar{\mathbf{a}}$ is defined by this method to capture the actual tangential displacement for each time step for use in calculating the correct dilatational pressure (last function given in Eq. 21).

In addition, the normal displacement increment is $\Delta \mathbf{g}_{N_{n+1}}^{i+1}$, which is equivalent to the following, noting that it is negative when in contact:

$$\Delta \mathbf{g}_{N_{n+1}}^{i+1} \equiv -\mathbf{N}^{\text{std}} \Delta \bar{\mathbf{a}} \cdot \mathbf{n}_{\Gamma_d}. \tag{27}$$

Note that the frictional coefficient μ is updated at every iteration for each time step according to Eq. 29.

2.8 Variation of Fault Permeability Due to Fault Aperture Change

To model the evolution of the hydraulic aperture from the initial value $2h_0$ with the increase in normal mechanical aperture change $\Delta 2h_m$ a lognormal aperture distribution was chosen, which uses the standard deviation of the surface roughness asperity heights σ_h (Renshaw 1995):

$$2h = 2h_0 + \Delta 2h_m \exp \left[-\ln \left[1 + \left(\frac{\sigma_h}{\Delta 2h_m} \right)^2 \right] / 2 \right]. \tag{28}$$

This relationship was selected, since:

- The close alignment of this theoretical relationship with published experimental data between mechanical and hydraulic apertures (Renshaw 1995) clearly indicates its applicability and accuracy.

- The parameter (the standard deviation of the non-logarithmized surface heights) used in this theory to describe the link between the hydraulic aperture and mechanical aperture change is physical and may be related to published values for natural discontinuities. This has an advantage over other published relationships (Kohl et al. 1995; Rutqvist 2015) that are purely empirical and, therefore, require calibration, and over other relationships (Kohl and Mège 2007) that are not mechanism-based and apply only to a specific site (no input parameters).
- The normal mechanical aperture change is used; therefore, when dilation is considered in the model, the link between shear slip and permeability of the fault is accurately captured. This is in contrast to using the effective normal contact stress to determine the change in hydraulic aperture (Kohl et al. 1995; Kohl and Mège 2007; Guglielmi et al. 2013; Rutqvist 2015), where these relationships cannot capture the increase in permeability due to shear slip.

3 Numerical Simulation of Fluid Injection into a Fault

We apply this model to represent fault reactivation during a well-constrained field experiment. The in-situ experiment monitors a natural but initially inactive fault in carbonates (southeastern France) which was reactivated through the high-pressure injection of water. The step-rate injection method for fracture in-situ properties (SIMFIP) probe (Guglielmi et al. 2013) was used for simultaneous measurement of fault-normal and fault-parallel displacements during fluid pressurization. The > 500 m long fault is accessed from an underground research laboratory at a depth of 282 m. The in-situ temperature was 12.5 °C at the location of the injection and did not change during the experiment—thermal effects are ignored. A vertical well intersects the fault with water injected into a 1.5 m long borehole zone between two inflatable packers that span the intersection with the fault zone (Fig. 3). A total of 950 l of water was injected with a step-increasing flow rate, while pressure, flowrate, fault relative displacements in both shear and dilation and seismicity were all measured and recorded (Guglielmi et al. 2015a). This experiment is to be reproduced via the coupled X-FEM numerical model.

3.1 Numerical Model

The grid size and density were selected following a mesh sensitivity analysis. The mesh was 50×51 elements in the x and y directions, respectively (see Fig. 4), with more elements in the y direction than the x direction so that the strong discontinuity (that is, the fault) crossed through the

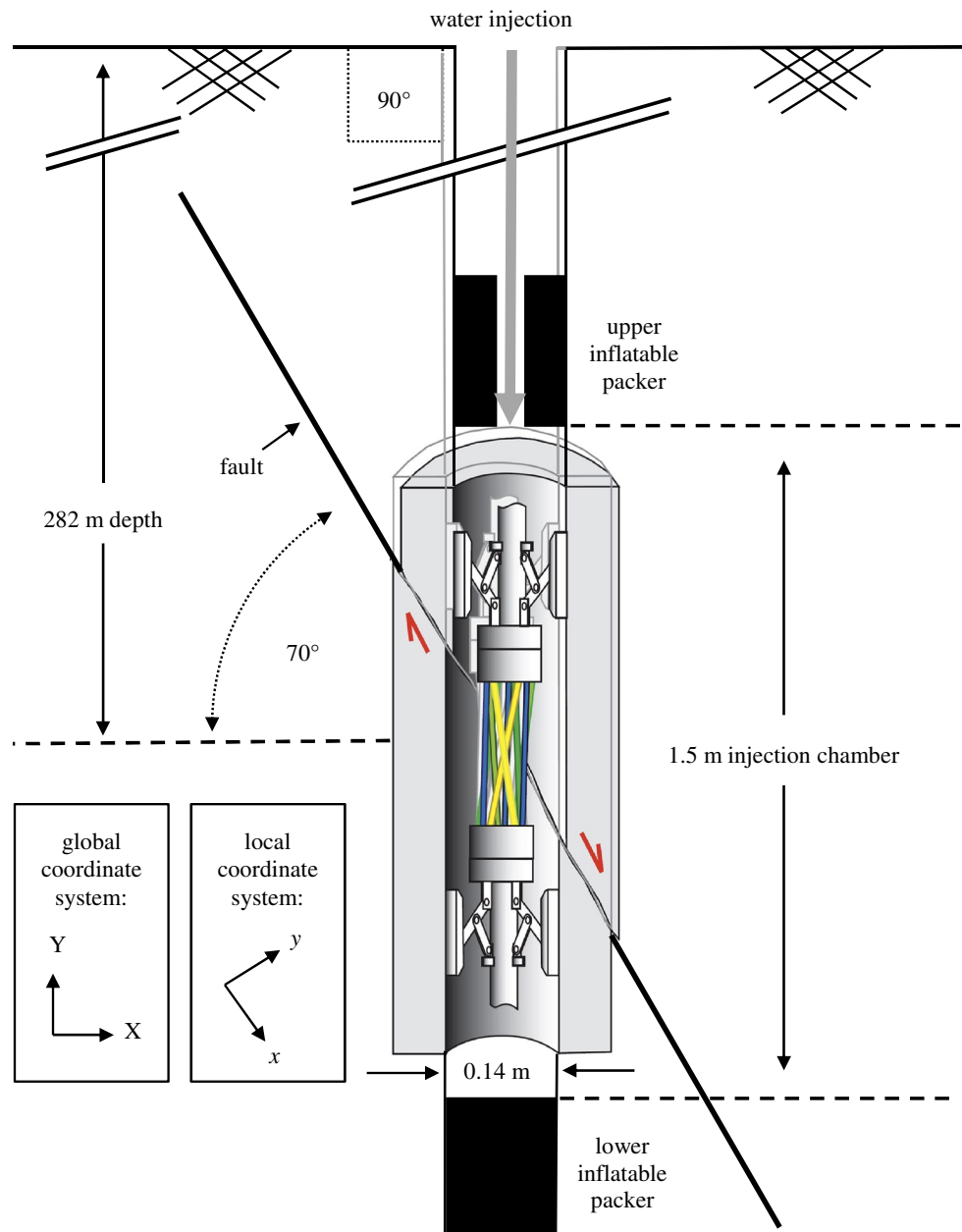
center of the elements. An even number of elements were chosen in the x direction so that the simulated fluid could be injected at the center of the model with this on the edge of two elements. The model dimensions are 250 m in both x and y directions. These dimensions were chosen based on the anticipated radius of the slip and pressurized zones recovered from previous modeling (Guglielmi et al. 2015a).

3.2 Boundary and Analysis Conditions

The effective in-situ stresses were $\sigma'_{xx} = -5.649$ MPa, $\sigma'_{yy} = -3.351$ MPa and $\sigma'_{xy} = 0.964$ MPa; and initial pore pressure was $p_0 = 2.764$ MPa (following the usual mechanics convention, negative values are compressive). These rotated effective stresses are required to rotate the fault (dip of 70° below horizontal towards 120°) to horizontal. The maximum, intermediate and minor principal stresses were measured to be -6.0 ± 0.4 MPa with a dip of 80° towards 300° (from north), -5.0 ± 0.2 MPa dipping 5° below horizontal towards 110° from the north, and -3.0 ± 0.1 MPa dipping 2° towards 200° from the north, respectively. Note that a plane strain condition is applied, but in reality, there is a -5.0 MPa (compressive) stress along the z -axis of the model. This stress does not contribute to the initial normal effective stress along the fault, which has an important role in the fault slip mechanism caused by fluid injection. However, the plane strain condition may overestimate the shear displacement magnitude due to the lack of constraint. In addition, the variation in accuracy of the far-field principal stresses has not been considered in the X-FEM model and the mean values alone are used. These in-situ stresses were only measured at the injection point; therefore, the gradient of stress is unknown. Body forces are used to account for the gradient of the in-situ stresses due to gravity. The initial pore pressure is based on a pore pressure gradient of approximately 9.801 kPa/m. Changes in pore pressure are driven by the injection of water at the center of the fault, with this influencing the mechanical deformation of the simulation. The body force vector has been rotated to represent the rotated vertical direction of the model. Since the boundaries are remote from the source of the fluid injection, they are pinned. A schematic representation of the model is shown in Fig. 5:

The model is run with a time increment (Δt) of 5 s. This time increment is the largest that produces a stable and consistent result. This was determined by varying the time step size until no changes in pressure and tangential and normal displacement resulted at the location of injection at the center of the model.

Fig. 3 Schematic of the in-situ experiment to be reproduced via X-FEM modelling (adapted from reference (Guglielmi et al. 2015b))



3.3 Flow Rate Input and Associated Assumptions

The flow rate for the in-situ experiment is first converted to cubic meters per second from liters per minute (see Fig. 6). Note that these values are taken from the supplementary material supplied by Guglielmi et al. (2015a).

At the core of the fault there would be multiple fractures accessed in the 1.5 m pressurized section of the in-situ experiment. Ten reference values were used to obtain the average and standard deviation for the fracture density near the fault core in a 1.5 m section. These 10 values were taken from previous studies on faults transecting carbonates

(Kostakioti et al. 2004; Niwa et al. 2009; Caine et al. 2010; Savage and Brodsky 2011; Guerriero et al. 2013; Ran et al. 2014; Meier et al. 2015; Choi et al. 2016). The number of fractures per meter was 56 ± 25 ; this is equivalent to 83 ± 37 fractures in the 1.5 m pressurized zone (rounding to the nearest integer). These measured values were used unaltered in the simulations to provide an unbiased representation of the predicted number of fractures (NoF) that would have been encountered in the in-situ experiment. The pressure increase at the injection section would, therefore, flow into multiple discontinuities. Thus, in these simulations the number of

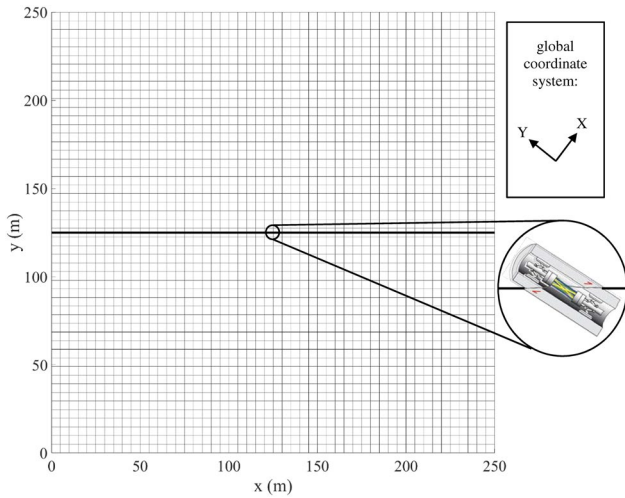


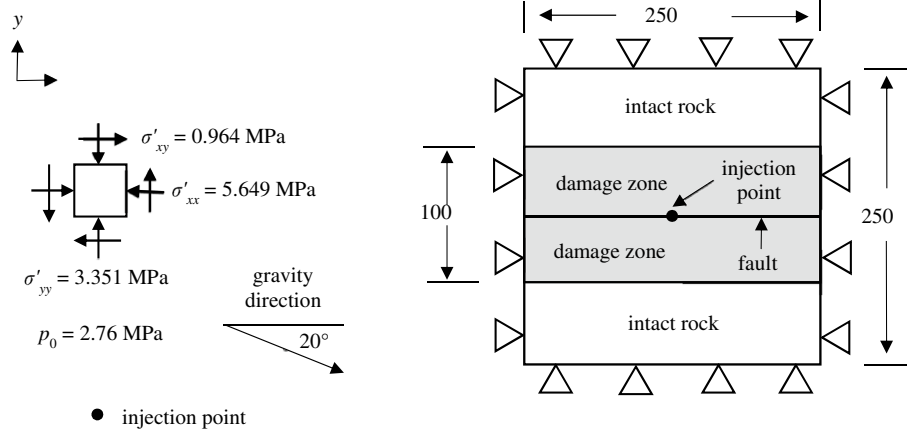
Fig. 4 Extended finite element mesh (the fault is the horizontal black line) with the packer orientation shown (the SIMFIP borehole tool is actually oriented in the vertical direction)

fractures in this 1.5 m pressurized section is assumed to range from 46 to 120 to capture the possible range for this fault. The two-dimensional model uses 1 m along the z direction; therefore, the cross-sectional area normal to flow of one fracture is simply the hydraulic aperture. The following expression converts the flow rate for all the fractures into a single fracture, which is used as direct input into the simulation (q in Eq. 10):

$$\text{flow rate}_{\text{one fracture}} = \frac{\text{flow rate}_{\text{all}}}{(\text{NoF})(2h)} \tag{29}$$

This flow rate is in meters per second as required. This simplification is required, since the X-FEM model would become unstable and/or extremely computationally intensive if up to 120 fractures were inserted into one row of elements.

Fig. 5 Schematic of fault and numerical model domain



Therefore, one strong discontinuity is used in this model to represent the in-situ fault.

The assumption of using one strong discontinuity is valid, since the apparent normal and tangential stiffness values are used to assist the calculation of the normal and shear displacements during the simulation. Apparent stiffness values are usually used to represent faults (Cappa et al. 2006; Guglielmi et al. 2008; Eftekhari et al. 2014; Konstantinovskaya et al. 2014). Therefore, this is a common assumption made in the literature. Since these stiffness values are estimated from the properties of the fault, the individual stiffness values must be estimated. Hence, there would be hardly any additional benefit of inserting up to 120 fractures in the model, based on the variability of the parameters. Therefore, using the apparent stiffness values allows for easier comparison with previous models.

In addition, the fracture distribution along the fault is impossible to represent exactly. These models assume that most of the fractures are parallel to the dip of the fault, but in reality, these discontinuities cross and terminate at different points along the fault, depending on the characteristics of the local geology. However, most faults have fractures that are orientated near parallel to the dip of the fault. At this stage, it is deemed reasonable to assume that the fractures are mostly parallel. This is due to the uncertainty in the number

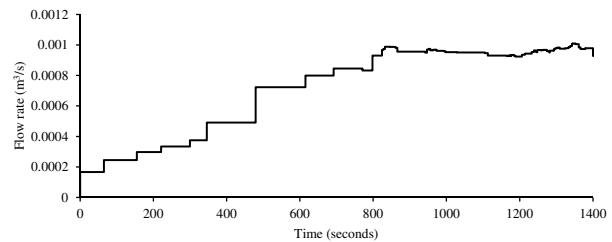


Fig. 6 Prescribed flow rate during the in-situ experiment

of fractures encountered in the 1.5 m long pressurized section, since this parameter was not reported.

To have some sense of the system (or apparent) stiffness for multiple discontinuities present at the fault core in the pressurized section, the following expressions are used to calculate the normal and tangential stiffnesses of a single two-dimensional discontinuity from the system stiffnesses, assuming 83 fractures in 1.5 m of the pressurized section (Yoshida and Horii 2004):

$$\bar{k}_N = \frac{2\bar{E}}{\pi L_N^d} \text{ and } \bar{k}_T = \frac{2\bar{G}(1 + \bar{\nu})}{\pi L_T^d}, \quad (30)$$

where L_N^d is the normal effective discontinuity length (m) and L_T^d is the tangential effective discontinuity length (m). These two values for effective lengths were assumed as double the average spacing value between discontinuities in the 1.5 m pressurized zone. Note that \bar{E} is the effective elastic modulus in a direction normal to the discontinuity (Pa), \bar{G} is the tangential effective shear modulus (Pa) and $\bar{\nu}$ is the effective Poisson's ratio for the system, which can be calculated by the following equations (Brady and Brown 2013):

$$\bar{E} = \left[\frac{1}{E} + \frac{1}{k_N S} \right]^{-1}, \bar{G} = \left[\frac{1}{G} + \frac{1}{k_T S} \right]^{-1} \text{ and } \bar{\nu} = \frac{\bar{E}}{E} \nu, \quad (31)$$

where S is the spacing (m) and G is the shear modulus of the damaged rock (Pa), which is calculated as $E/2(1 + \nu)$. Note that the calculated stiffness values for the single discontinuity were assumed to be constant when changing the number of fractures in the 1.5 m long pressurized section.

The system stiffness varies with the number of fractures as this parameter changes the average spacing. It was found for the mean values that the maximum absolute relative change of stiffness, when varying the number of fractures from 83 to 46 fractures, was approximately 8.5%. The maximum absolute relative change in the apparent stiffness values between the upper and mean values, and between the lower and mean values, in this study was approximately 62% thus encompassing the range of stiffnesses expected. Given that the variations in stiffness due to the number of fractures are significantly smaller than the uncertainty associated with the apparent (or system) normal stiffness and tangential stiffness values, these stiffness values were not changed when the number of fractures altered, but were able to be varied in the sensitivity analysis and calibration process.

In addition, the fault permeability is not varied when the number of fractures changed in the pressurized region. This is since the absolute relative range from the mean values is approximately 111% when comparing the change in the number of fractures from 83 to 46 fractures and 120 fractures, whereas the absolute relative range from the mean values to the lower and upper values is approximately 506% for

the hydraulic aperture. Therefore, the change in the number of fractures is considered insignificant when compared to the uncertainty in the hydraulic aperture of the fault. Therefore, the fault permeability was able to be varied in the calibration process but was not changed when the number of fractures was altered. Note that aperture values are taken from published in-situ values for faults. Therefore, the number of fractures is implicitly considered in these published in-situ back-calculated values. However, the number of fractures encountered in the pressurized zone of the experiment would change the hydraulic aperture of the fault, which can readily be accounted for in our coupled X-FEM model. Hence, this is not a limitation of the model, since when calibrating the model, the change in number of fractures in the pressurized zone can be linked with the hydraulic aperture of the fault, if required.

4 Model Sensitivity Analysis

The mechanical and transport properties of the rock and fault control the magnitude and distribution of pore pressures and the evolving magnitude of slip and normal displacement change. Thus, to give a better understanding of how the ranges of each parameter (expected for this fault traversing the carbonate) changes the base case (with the mean values), a sensitivity analysis was conducted.

4.1 Range of Input Parameters

Values for each parameter were obtained with the mean value used for the base case and the lower and upper bound cases defined as offset by a single standard deviation. If the value was infeasible (outside the range of reasonably allowable values), then it was adjusted to the closest reasonable value. In this manner, only the kappa value (representing the deviation from parallelism of the fault faces—see Sect. 2.4 for its definition) for the lower bound case was adjusted to be the lowest feasible value. In addition, the mean value of the apparent tangential/shear stiffness value was increased from 6.8 to 13.0 GPa/m, to avoid the lower value (minus one standard deviation) being close to zero. The same standard deviation was used to alter the upper and lower values for the apparent tangential stiffness. Note that the apparent normal and tangential stiffnesses are taken only from published values for in-situ carbonate faults, which include multiple fractures within the fault core. Adjustment of these apparent stiffness values were not required due to the assumed number of fractures encountered in the pressurized zone of the experiment, since they inherently incorporate the contribution of the overall in-situ fault, with multiple fractures that concentrate at the fault core. It was found for the

cases presented that the maximum absolute relative change of stiffness, both normal and tangential, was insignificant with respect to the uncertainty in material properties (see Sect. 3.3 for the discussion). Therefore, no change in the apparent published stiffness values is applied when the number of fractures is altered in the sensitivity analysis and calibration process; since these values include the influence of multiple fractures encountered in a fault and the calculated change in number of fractures was insignificant compared to the uncertainty in these stiffness values.

The model includes a damage zone extending 50 m from the fault with higher permeability than the surrounding rock mass. This damage zone width was chosen based on the approximate median value from 18 reference datasets (Torabi et al. 2020). This is deemed a reasonable value, since fault damage zones may extend 3 m–200 m from the fault core (Billi et al. 2003), depending on the fault shear displacement. The damage zone has been shown to have a significantly higher permeability (approximately 10^5 times more) than the surrounding intact rock (Micarelli et al. 2006; Agosta et al. 2007).

The variation in rock parameters representing the mean, lower and upper values are presented in Table 1.

The elastic modulus of the damage zone was changed to half that of the intact rock, according to field measurements at the experimental site (Guglielmi et al. 2015a).

The properties of the fault that were varied (mean, lower and upper) are reported in Table 2.

The fault is represented by the rate state formalism of Eq. 18. Modelling for the in-situ experiment (Guglielmi et al. 2015a), demonstrated that the inclusion of the “state” part of this constitutive relationship (in Eq. 18) did not improve the prediction of slip movement during this experiment, at least within the uncertainty of the measurements (Guglielmi et al. 2015a). Hence, the same modified frictional law was used in the X-FEM simulations:

$$\mu = \mu_0 + a \ln \left(\frac{V}{V_0} \right). \quad (32)$$

The reference velocity (V_0) was assigned a value of 1×10^{-7} m/s (Guglielmi et al. 2015a). This rate (state) frictional law, therefore, can vary the frictional coefficient, depending on the velocity experienced at that point along the fault, where the base frictional coefficient was assumed constant over the length of the fault. Note that the laws proposed by Dieterich and Ruina are identical when excluding the evolution of state (Dieterich 1979; Ruina 1983).

Table 1 Rock parameters representing the mean values with parameters for lower and upper values offset by a single standard deviation

Parameter	Mean	Lower	Upper	References
Intact elastic modulus E (GPa)	31.3	12.8	49.7	Bell (2013)
Poisson's ratio ν	0.30	0.25	0.35	
Density ρ_s (kg/m ³)	2364	2225	2503	
Porosity n (%)	14.8	8.1	21.6	
Biot poroelastic constant α_{Biot}	0.77	0.75	0.79	Lion et al. (2004, 2005); Da Silva et al. (2010)

Table 2 Fault parameters representing the mean values with parameters for lower and upper values offset by a single standard deviation

Parameter	Mean	Lower	Upper	References
Fault damage zone permeability k_f (m ²)	2.71×10^{-14}	4.83×10^{-15}	4.93×10^{-14}	Micarelli et al. (2006); Agosta et al. (2007)
Fault damage zone width (m)	50	10	100	Torabi et al. (2020)
Initial hydraulic aperture $2h_0$ (m)	5.57×10^{-5}	1.39×10^{-5}	9.75×10^{-5}	Guglielmi et al. (2008, 2015b)
κ parameter	1.2	1.0	1.5	Witherspoon et al. (1980)
Apparent normal stiffness \bar{k}_N (GPa/m)	31.8	12.0	51.6	Cappa et al. (2006); Guglielmi et al. (2008); Eftekhari et al. (2014); Konstantinovskaya et al. (2014)
Apparent tangential stiffness \bar{k}_T (GPa/m)	13.0	6.3	19.7	
Dilation angle φ_d (°)	10	0	20	–
Frictional coefficient μ_0	0.61	0.50	0.72	Nagata et al. (2012); Guglielmi et al. (2015a)
a parameter	2.5×10^{-2}	0	5×10^{-2}	
Standard deviation of non-logarithmized fracture asperity heights σ_h (m)	2.5×10^{-4}	0	5.0×10^{-4}	Renshaw (1995)

All other parameters are taken as constant for each case. The permeability of the intact rock mass was $6.77 \times 10^{-19} \text{ m}^2$ (Agosta et al. 2007). The permeating fluid was water at approximately room temperature; hence, the dynamic viscosity μ_{fd} was $8.9 \times 10^{-4} \text{ Pa}\cdot\text{s}$, the fluid bulk modulus K_f was 2.15 GPa and the fluid density ρ_f was approximately 999.4 kg/m^3 .

4.2 Influence of Each Parameter on the Fluid-Mechanical Coupling Behavior of the Fault

To investigate the influence of each parameter on the closeness of fit to the measured data, a sensitivity analysis was conducted. This sensitivity analysis changed only one parameter at a time to the lower then upper bounding value (given in Sect. 4.1, Tables 1 and 2). The closeness of fit was calculated by a weighted objective function. The objective function is the sum of the squared residuals (difference between the measured and modelled values) multiplied by a

weight. The lower the weighted objective function the closer the fit to the data. These weights were calculated based on each observation set (pressure, shear displacement, and normal displacement) having an equal contribution to the weighted objective function, where the residual is defined from the deviation from the measured average value for each group. The weights for the pressure, shear displacement and normal displacement observation sets were 0.2565, 0.8570, and 1.1464, respectively. These weights were calculated by initially setting each of these weights to one then minimizing the difference between the weighted objective functions of each three categories (pressure, shear displacement, and normal displacement). The weighted objective functions for each category are the residual from the average of the dataset multiplied by the weight then squared and summated. This results in an unbiased weighted objective function. The results in Fig. 7 indicate the change of the weighted total objective function from the mean value case (where in the legend they are listed from the greatest amount of change in the weighted objective function to the least).

How each parameter influences the groups (i.e., pressures, shear and normal displacements) is shown in Fig. 8. The most sensitive parameters are summarized below and the least sensitive parameters are summarized in the Appendix. The most sensitive parameters are listed, in order, from the greatest influence on the weighted objective function to the least. In addition, the mechanisms that change the pressures, shear displacements, and normal displacements are given.

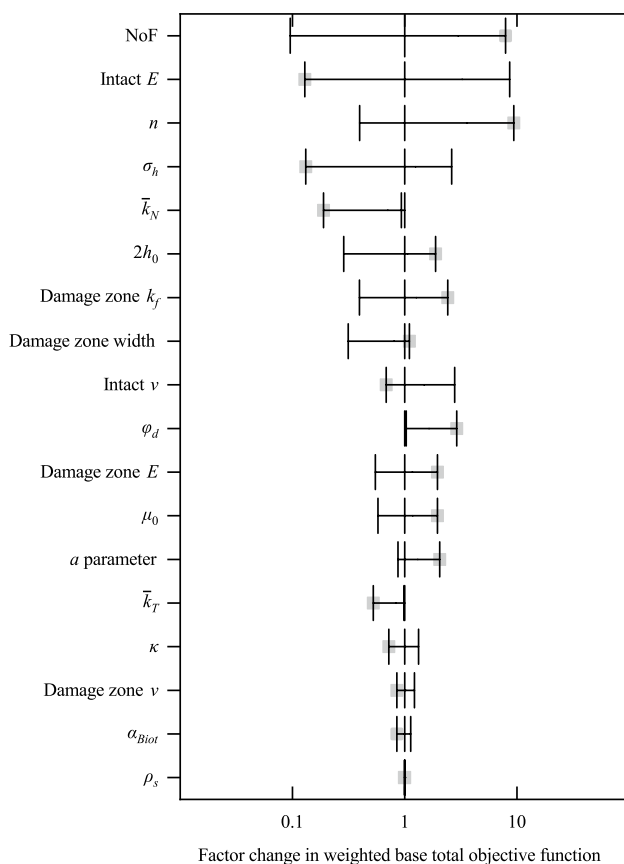


Fig. 7 Sensitivity analysis results showing the ratio of the change in the weighted total objective function from the base case for each parameter (with the solid square symbolizing minus one standard deviation, the base case having a value of one, and plus one standard deviation offset from the base case)

- Number of fractures (NoF)

The parameter that affects the weighted objective function the most is the number of fractures, since this directly changes the amount of flow into the single representative strong discontinuity (see Eq. 29). Since the fracture density near the fault core was not reported, previously published values from representative carbonate faults were used. This results in a necessarily large range for the number of fractures. Increasing the number of fractures produces lower flow through the fault core, reducing the pressure and displacements (for both normal and shear components).

- Intact elastic modulus (E)

The second most influential parameter on the weighted objective function is the intact elastic modulus, since this parameter changes the overall coupled response of the (porous) rock mass. That is, when there is a higher intact elastic modulus both the pressure and displacements (for both normal and shear components) increase. This is expected, since flow is only introduced at the center of the fault and depending on how ‘stiff’ the rock mass is, changes how the fault responds. In addition, since the range is based on non-site specific carbonate rocks it is

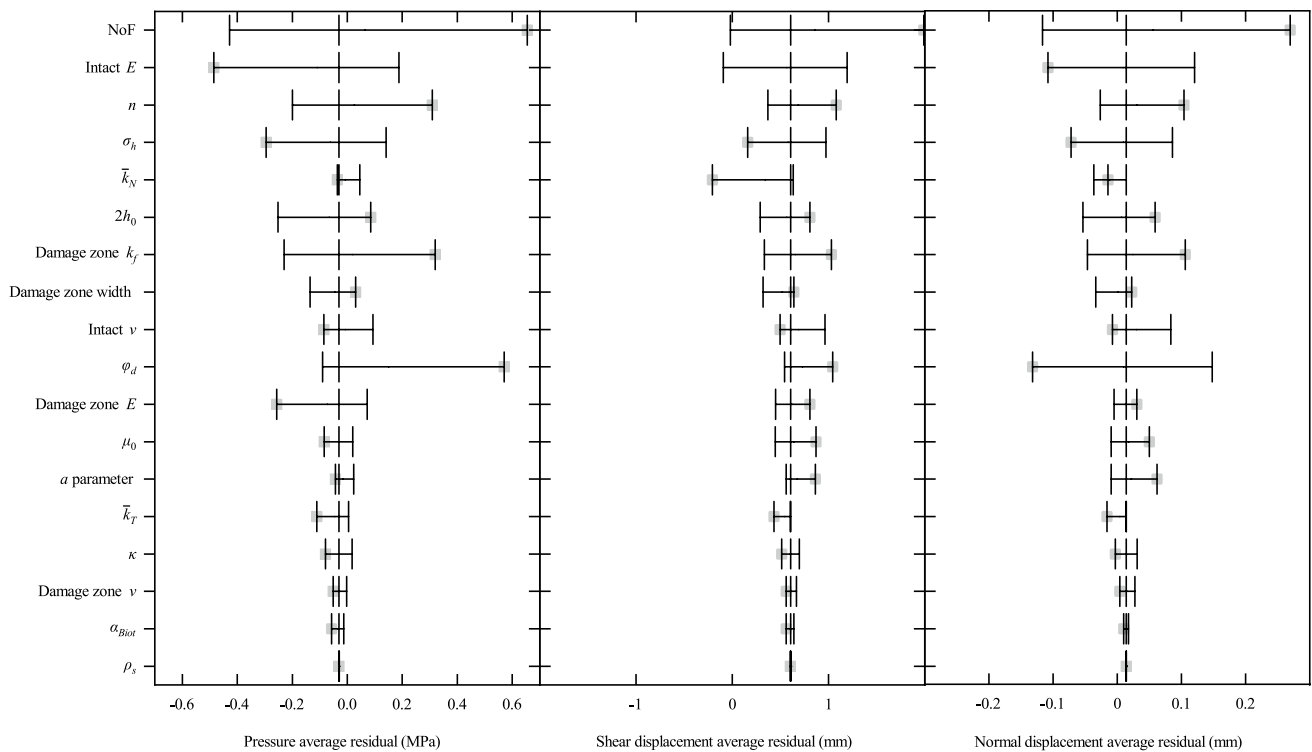


Fig. 8 Average residual values for the pressure, shear displacement, and normal displacement categories when changing each parameter independently (with the solid square symbolizing minus one standard

deviation, the base case all being the same value, and plus one standard deviation offset from the base case)

expected this range is higher than what was encountered in the actual in-situ experiment.

- Porosity (n)

The lower the porosity the less fluid volume needed to create pressure along the fault, resulting in higher pressure and displacements (in both normal and shear components). Since the porosity was estimated based on non-site specific carbonate rocks, it is expected that the range used is higher than that for the rock mass in the in-situ experiment. Therefore, this porosity range would affect the sensitivity result of the weighted objective function.

- Standard deviation of non-logarithmized fracture asperity heights (σ_h)

The standard deviation of non-logarithmized fracture asperity heights (that is, a measure of the roughness) changes the relationship between the opening of the fault and the hydraulic aperture, and hence the permeability along the fault. The more planar the fracture surface, the closer this parameter to zero and the closer the changes in hydraulic aperture to the opening displacement of the fault. Hence, the lower limit of zero means that the fault becomes more permeable which results in a lower pressure at the center of the fault, and less overall displacement (in both shear and normal components).

- Normal stiffness (\bar{k}_N)

The impact of the normal stiffness is similar to that of the intact elastic modulus, in that the higher the value the greater the fluid pressure produced and hence the greater the resulting displacement (for both normal and shear components). This parameter exerted less influence on the weighted objective function than the intact elastic modulus.

- Initial hydraulic aperture ($2h_0$)

The higher the initial hydraulic aperture, the greater the increase in permeability along the fault that produces lower pressures along the fault, which results in less movement (in both the normal and shear directions).

- Damage zone permeability (k_f)

The higher the permeability of the damage zone the greater the fluid pressure dissipation and the lower the resulting pressure along the fault which, in turn, reduces the displacement magnitudes (in both normal and shear directions).

- Damage zone width

The greater the damage zone width the lower the pressure along the fault, since there is a larger region responding with the equivalent elastic modulus of the damage zone, producing a less ‘stiff’ system. The lower pressure along the fault produces less movement (in both the normal and shear directions).

- Intact Poisson's ratio (ν)
The higher the intact Poisson's ratio the larger the displacement at the injection point (that is, the center of the fault), while the fluid pressure remains similar for the sensitivity analysis. This may result, since the compressive stress along the fault is larger than that across the fault. This would provide additional force from the along-fault in-situ compressive stress, which may generate higher displacements from the larger intact Poisson's ratio value.
- Dilation angle (φ_d)
The higher the dilation angle the lower the fluid pressure, which produces less shear displacement but increases the normal displacement. The higher the dilation angle, the greater the normal displacement resulting from shear slip.
- Damage zone elastic modulus (E)
The lower the damage zone elastic modulus the less stiff the overall simulated fault system. This results in lower pressure along the fault, but more displacement (in both normal and shear directions), since it requires a lower stress to induce the same displacement.

5 Verification of the X-FEM Code

The X-FEM code was verified using history matching. History matching is a type of inverse problem in which the observations in the reservoir (pressures and displacements in the present study) are used to estimate model variables that caused that response. History matching parameterizes the model and assists with the subsequent prediction of future reservoir response. History matching implies that a model of the reservoir has parameters that have some physical interpretation and assigns these values such that the model optimally reproduces the observed measurements (that is, in the present study, from the in-situ experiment). History matching problems are usually ill-posed with many possible parameter combinations that result in equally good matches to the past observations (Oliver and Chen 2011).

The parameter estimation (PEST) software suite was used to conduct the history matching process. The PEST software suite is a frequently used tool for highly parameterized model calibration. The PEST software suite is open-source and in the public domain. The main purpose of the PEST software suite is to estimate parameters in models from history matching, and conduct parameter/predictive-uncertainty analysis. This software is widely used in groundwater and surface water parameterization (Doherty and Hunt 2010). However, it has been linked to other software such as Code_Aster, a finite element code used to model hydrothermal circulation at a geothermal site in France (Vallier et al. 2018), and the TOUGH2 suite of non-isothermal multiphase

flow simulators which already had calibration capacity using iTOUGH2 (Finsterle and Zhang 2011).

5.1 Calibration of Parameters Using the PEST Software

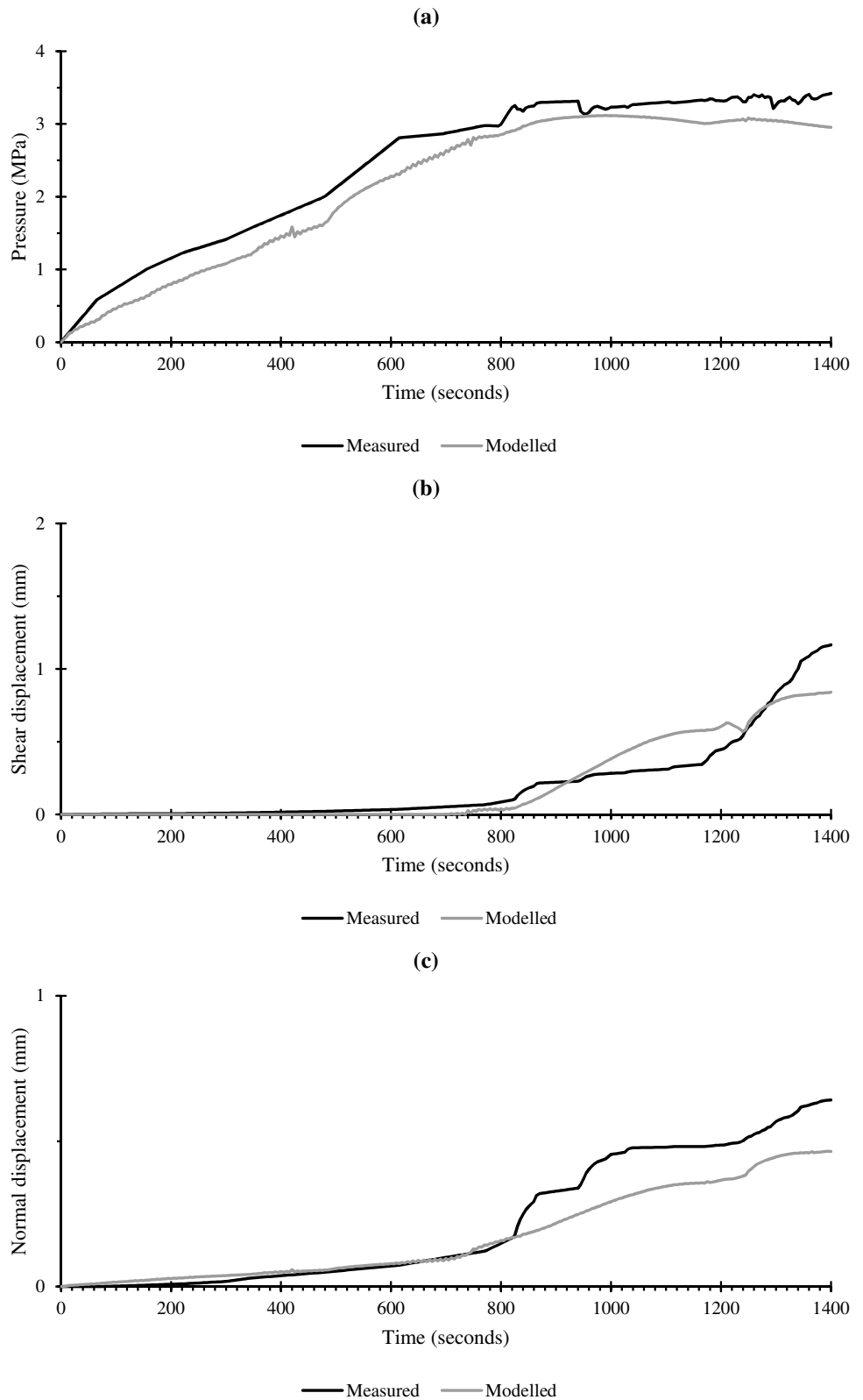
The Levenberg–Marquardt algorithm (Moré 1978) is used in PEST to reduce the objective function, which is the summation of the squared weighted residuals. The smaller the objective function the closer the overall fit to the measurements. Using the mean case values with 83 fractures, the initial weighted objective function was 179.15, with individual contributions from the pressure, shear displacement, and normal displacement measurement groups of 0.33, 178.38, and 0.44, respectively. This corresponded to a coefficient of determination (R^2) of 0.3398 and a ratio of 0.5697 between the normalized measured data and the normalized modelled values (which corresponds to an overestimation). The observation measurements of the pressure, and shear and normal displacements for every 5 s were given weightings of 0.2565, 0.8570, and 1.1464, respectively (see Sect. 4.2 for how this was calculated). These weightings alter the total objective function to reflect the measured values magnitudes. The observation measurements were linearly interpolated from the published data to obtain values for every 5 s up to 1,400 s.

The PEST calibration process reduced this initial objective function to 6.55 (approximately 3.7% of the initial weighted objective function), with individual contributions from the pressure, shear displacement and normal

Table 3 Comparison between initial and calibrated parameters

Parameter	Initial	Calibrated
Damage zone elastic modulus E (GPa)	15.6	16.2
Damage zone Poisson's ratio ν	0.30	0.34
Intact zone elastic modulus E (GPa)	31.3	29.2
Intact zone Poisson's ratio ν	0.30	0.33
Density ρ_s (kg/m ³)	2364	2364
Porosity n (%)	14.80	14.25
Fault damaged zone permeability k_f (m ²)	2.71×10^{-14}	4.93×10^{-14}
Biot poroelastic constant α_{Biot}	0.77	0.77
Initial hydraulic aperture $2h_0$ (m)	5.57×10^{-5}	4.79×10^{-5}
Kappa factor κ	1.2	1.2
Apparent normal stiffness \bar{k}_N (GPa/m)	31.8	27.7
Apparent tangential stiffness \bar{k}_T (GPa/m)	13.0	11.5
Dilation angle φ_d (°)	10	19
Frictional coefficient μ_0	0.61	0.68
a parameter	2.5×10^{-2}	2.69×10^{-2}
Number of fractures	83	83
Standard deviation of non-logarithmized fracture asperity heights σ_h (m)	2.5×10^{-4}	1.9×10^{-4}

Fig. 9 **a** Pore pressure, **(b)** tangential displacement, and **(c)** normal displacement at the center of the model (injection point) over time for calibrated model



displacement measurement groups of 1.60, 2.26, and 2.68, respectively (using the same weightings for each observation group). Using the calibrated parameters, the R^2 value was 0.9480 and a ratio of 1.1288 between the normalized measured data and the normalized model values (corresponding to an underestimation) and representing a good match. Note that the lower and upper values were used as bounds for the estimation process. For a comparison of the calibrated and initial case parameters, see Table 3.

From Sect. 4.2, the analysis is most sensitive to the number of fractures, however; this value did not change from 83 fractures in the calibration. It is reasoned that this parameter did not change in the calibration, since an increase in its value decreases the fluid pressure and displacements and vice versa; meaning that the resultant change in the groups are interdependent. Note the other parameters that did not change in the calibration process were three out of the four

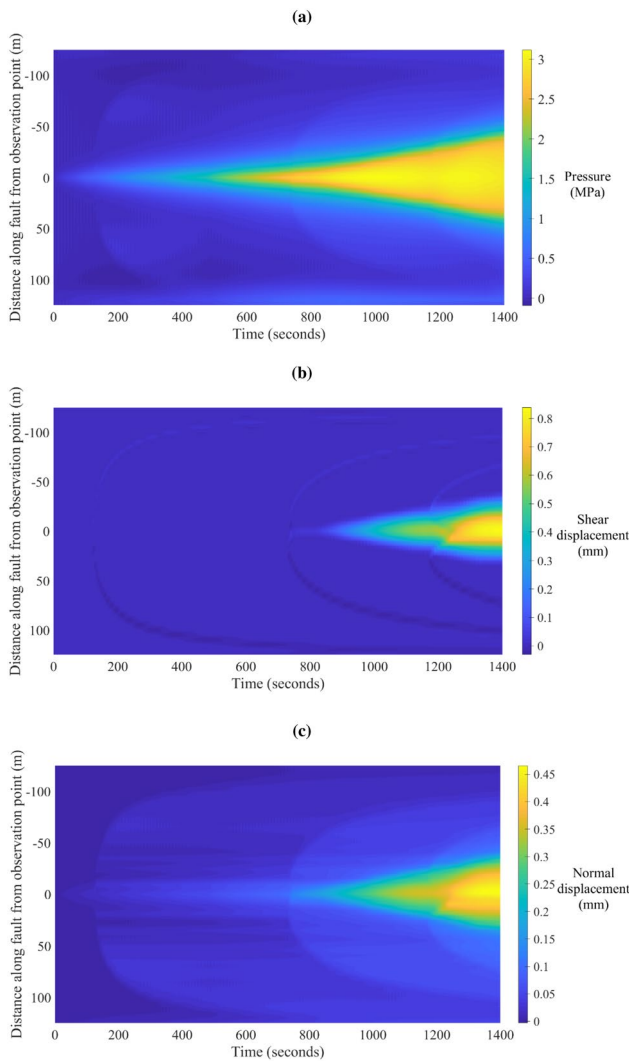


Fig. 10 a Pore pressure, (b) tangential displacement, and (c) normal displacement along the fault versus time for the calibrated model

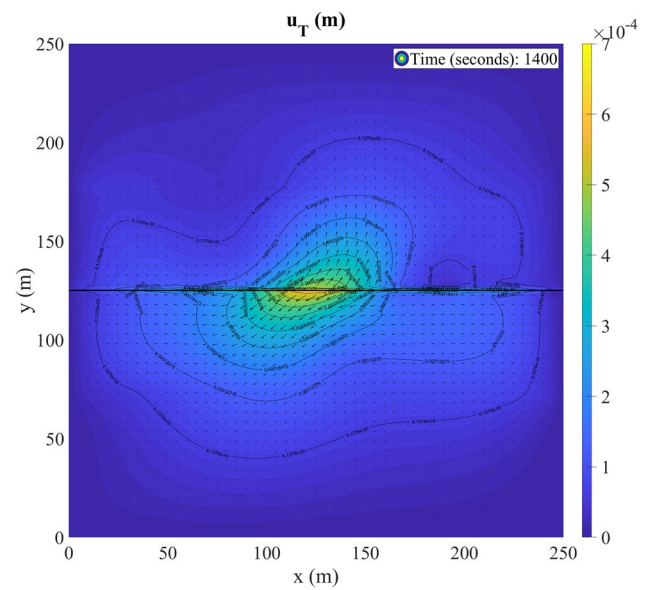


Fig. 11 Total displacement field for calibrated model at 1,400 s

least sensitive, as expected. In addition, the dilation angle, which lowers pressure and shear displacement while increasing the normal displacement, is most likely cause why this parameter changed significantly during the calibration.

5.2 Simulation Result with Calibrated Parameters

Figure 9 illustrates the change in the results from the initial to calibrated values, compared to the measured in-situ data. This illustrates that the choice of initial parameters was

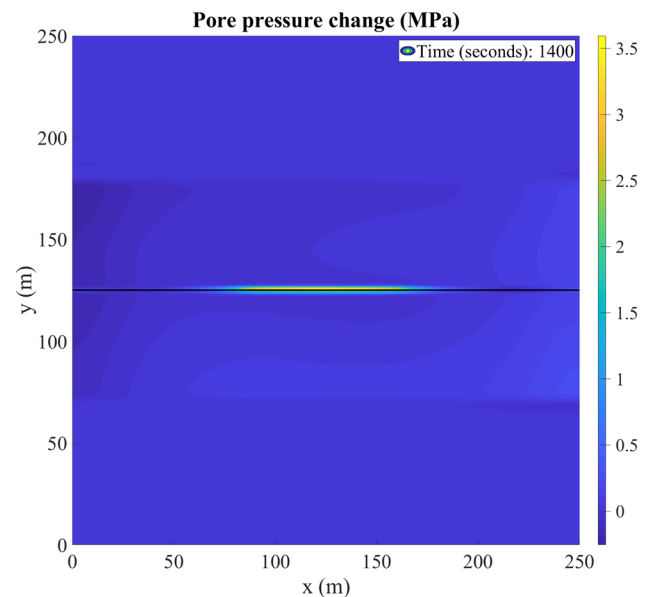


Fig. 12 Change in pore pressure for calibrated model at 1400 s

close to optimal for this coupled X-FEM model. Therefore, this illustrates the importance of either measuring or estimating appropriate parameter values for the fault system. Figure 10 shows the pore pressure, tangential displacement, and normal displacement over the fault versus time for the calibrated model. This illustrates that the extent of pore pressure migration is larger than the zone undergoing shear displacement in this model. Note that positive values from the injection (observation) point are deeper. See Fig. 11 for the total displacement field for the calibrated model at 1400 s and Fig. 12 for the change in pore pressure from the start of fluid injection for the calibrated model at 1400 s. This illustrates that the change in movement occurs close to the injection point at the center of the model.

5.3 Comparison with calibrated fault permeability with in-situ measurement

Based on in-situ measurements the fault zone had an average initial permeability of $7 \times 10^{-12} \text{ m}^2$ (Guglielmi et al. 2015a). This initial permeability corresponds to a hydraulic aperture of approximately $4 \times 10^{-5} \text{ m}$, which is close to the calibrated initial hydraulic aperture of $4.79 \times 10^{-5} \text{ m}$. This illustrates that via calibration, the initial hydraulic aperture and hence fault permeability, approaches the average of the in-situ measurements of the initial permeability of the fault zone.

6 Discussion

A critical review of the X-FEM approach presented in this study is provided in this section. This X-FEM technique is compared to conventional numerical simulation techniques, then the importance of fluid exchange between the fault and the rock is illustrated, and further development of this X-FEM approach is considered.

6.1 Comparison to Conventional Numerical Simulation Techniques

The X-FEM approach was shown to be a promising numerical method in this study to model fault slip, not only because of the in-situ experiment data falls in between the simulated range results, but for the following inherent features of this modelling technique:

1. A fully coupled approach that considers fluid exchange between the discontinuity and the rock, as well as along the fault is realized by the enriched shape functions.
2. A simple mesh can be implemented, whereby the discontinuity is not required to conform to the mesh geometry.

3. The influence of the discontinuity (in terms of the displacement and pressure fields) is accounted for in the framework of continuum mechanics.
4. Memory use is reduced, since only the elements that have the fault passing through them are enriched.

Various coupled numerical simulation techniques have been introduced to model fault slip, such as: linking the fast Lagrangian analysis of continua (FLAC) with TOUGH2—a multiphase flow simulator; coupled poroelastic FEM models; a coupled displacement discontinuity method (DDM); and the coupled distinct element method (DEM). These techniques are described below and compared to the X-FEM model presented in this study.

One notable simulation technique is the coupled multiphase fluid flow and geomechanical simulator Tough–FLAC (Rutqvist et al. 2002). This simulation method is based on the linking of the multiphase fluid flow simulator TOUGH2 (Pruess et al. 1999) and the geomechanical code FLAC^{3D} (Itasca Consulting Group 1997). TOUGH2 solves mass and energy balance equations that describe fluid and heat flow in general multiphase, multicomponent systems. Fluid transport is described with a multiphase extension of Darcy's law. Heat flow is induced by conduction and convection (Pruess et al. 1999). TOUGH2 assumes the pore pressure gradient is continuous, while in X-FEM, this gradient is discontinuous normal to the discontinuity. Using the TOUGH–FLAC simulator, fault slip analysis can be carried out either as a continuum analysis or fault analysis. The fault analysis utilizes the FLAC^{3D} mechanical constitutive model or interface elements and the continuum analysis is based around a failure criterion that determines the potential for fault slip with the evolution of the in-situ stresses. One of the reasons continuum analysis using TOUGH–FLAC is used, is if the location and orientation of the discontinuities in the field are not well known. It is suggested that it is useful, as a precaution, to assume the fault (or discontinuity) could exist at any point with an arbitrary orientation to determine whether the conditions exist for fault slip due to the evolving in-situ effective stresses. Contrarily, the fault analysis is used when the orientation of the fault is known. This can use either the mechanical interfaces or equivalent continuum representation using solid zones, or a combination of these two techniques. The mechanical interface is used if the thickness of the fault is negligible compared to the size of the problem. Interface elements are more difficult to implement, due to the gridding required by FLAC^{3D} and TOUGH2 and the associated coupling procedure (Rutqvist et al. 2007). In comparison to the TOUGH–FLAC simulation technique, the X-FEM model presented in this study provides an alternative to using the discrete fault analysis. This fully coupled X-FEM model makes the gridding and the coupling procedure easier due to the inbuilt functionality of this numerical

modelling technique. Therefore, this X-FEM approach can simulate fault slip due to fluid injection efficiently using a similar method to the TOUGH–FLAC simulator.

Another simulation technique was using the software package ABAQUS, by developing a plane strain poroelastic FEM model to simulate the time-dependent distributions of pore pressure and effective stress in each of the geological layers. In the simulation, the fault is represented as an embedded interface with zero thickness and mechanical properties equal to those of the surrounding formations, which allows fluid flow (Fan et al. 2016). In addition, a FEM code (PyLith) was coupled with a multiphase flow simulator (GPRS) which was used to simulate quasi-static fault slip. Similar to the model presented in this study, they incorporated a rate and state dependent friction model. However, there was no experimental validation (Jha and Juanes 2014). These FEM simulation techniques rely on the automatic mesh generation of the fault and the multiple geological layers. Whereas the coupled X-FEM model (in this study) uses a uniform mesh with quadrilateral elements (see Fig. 4) and a strong discontinuity (that does not need to conform to the mesh), which may provide a computationally more efficient method to represent a fault.

The DDM has been used to model fault slip with a focus on the three-dimensional coupled response (that is, fluid flow and thermal stress) in an enhanced geothermal reservoir (Ghassemi et al. 2007), where the rock mass is considered impermeable. As far as the authors are aware, the surrounding rock mass in DDM models is generally considered homogenous and linear, whereas the X-FEM approach can comprise different elastic properties. In addition, as mentioned in Sect. 3, the temperature did not change during the in-situ experiment; therefore, thermal stresses were not taken into account in the X-FEM model. However, this X-FEM approach has the capability to be extended to take into account thermal stress (Khoei 2014).

It is worthwhile to mention that the rate and state friction model has also been implemented in the DEM, where they investigated one and two block systems (Lorig and Hobbs 1990). Subsequent DEM models were able to perform coupled hydro-mechanical analysis to model fluid flow through a network of fractures, however; the blocks in these models are impermeable (Zangeneh et al. 2014). Hence, this DEM approach disregards the importance of fluid exchange between discontinuities and the rock material.

In summary, there are several different coupled numerical modelling techniques used to model fault slip including FLAC with TOUGH2; coupled FEMs; coupled DDMs; and coupled DEMs. However, they all have limitations and weaknesses associated with these approaches. This X-FEM approach has benefits over these approaches, however; its main disadvantage is the potential numerical instabilities that can be caused by an ill-conditioned Jacobian. Note these

issues were not encountered in this study due to the preconditioning scheme (Béchet et al. 2005) and the simplified geometry of the fault with respect to the mesh.

6.2 Importance of Fluid Exchange Between the Fault and The Rock

The fluid exchange between the fault and the rock plays a pivotal role in the simulation of fluid-induced fault-slip. The significance can be illustrated by comparing the range of movement (shear and normal) and pressure generated at the center of the fault between the impermeable and permeable cases using the X-FEM model. The impermeable case can be reproduced by setting the permeability of the rock (damage and intact zones) in the X-FEM model to zero.

Subsequently, as described in a later section, the impermeable X-FEM lower bound model, not using rate-state friction (i.e., using a constant frictional coefficient throughout the simulations), was compared to the Universal Distinct Element Code (UDEC) commercial software (Cundall 1980) results for the same parameters. This further examines the importance of the fluid exchange in the quantitative estimation of fluid-induced fault movement (Zhang and Sanderson 1996; Zangeneh et al. 2014; Khademian et al. 2018).

6.2.1 Comparison Between Impermeable and Permeable Cases Using X-FEM

To contrast the impermeable and permeable conditions two models were simulated (see Fig. 13). When the surrounding rock is impermeable, the fluid pressure increase at the center of the model is higher than the permeable case. This is expected, since the flow rate is the same but there is less fluid dissipating capability, hence resulting in higher pressure at the injection point (see Fig. 13a). As shown in Fig. 13b, in the impermeable case, more pressure causes greater slip along the fault. The normal displacement modelled results, shown in Fig. 13c, indicate that without considering fluid exchange these displacements are higher than when considering fluid exchange with the permeable case. Hence, consideration of fluid exchange produced a much closer simulated result for the in-situ experimental data studied. This indicates that fluid exchange between the fault core and the rock mass is an important mechanism that should be considered to model more accurately fault shear slip. The change in pore pressure, tangential displacement, and normal displacement along the fault over time for the impermeable case and using the calibrated values is shown in Fig. 14. This illustrates that the shear displacement is concentrated around the injection point. However, since the surrounding material is impermeable, the pressure migrates further when

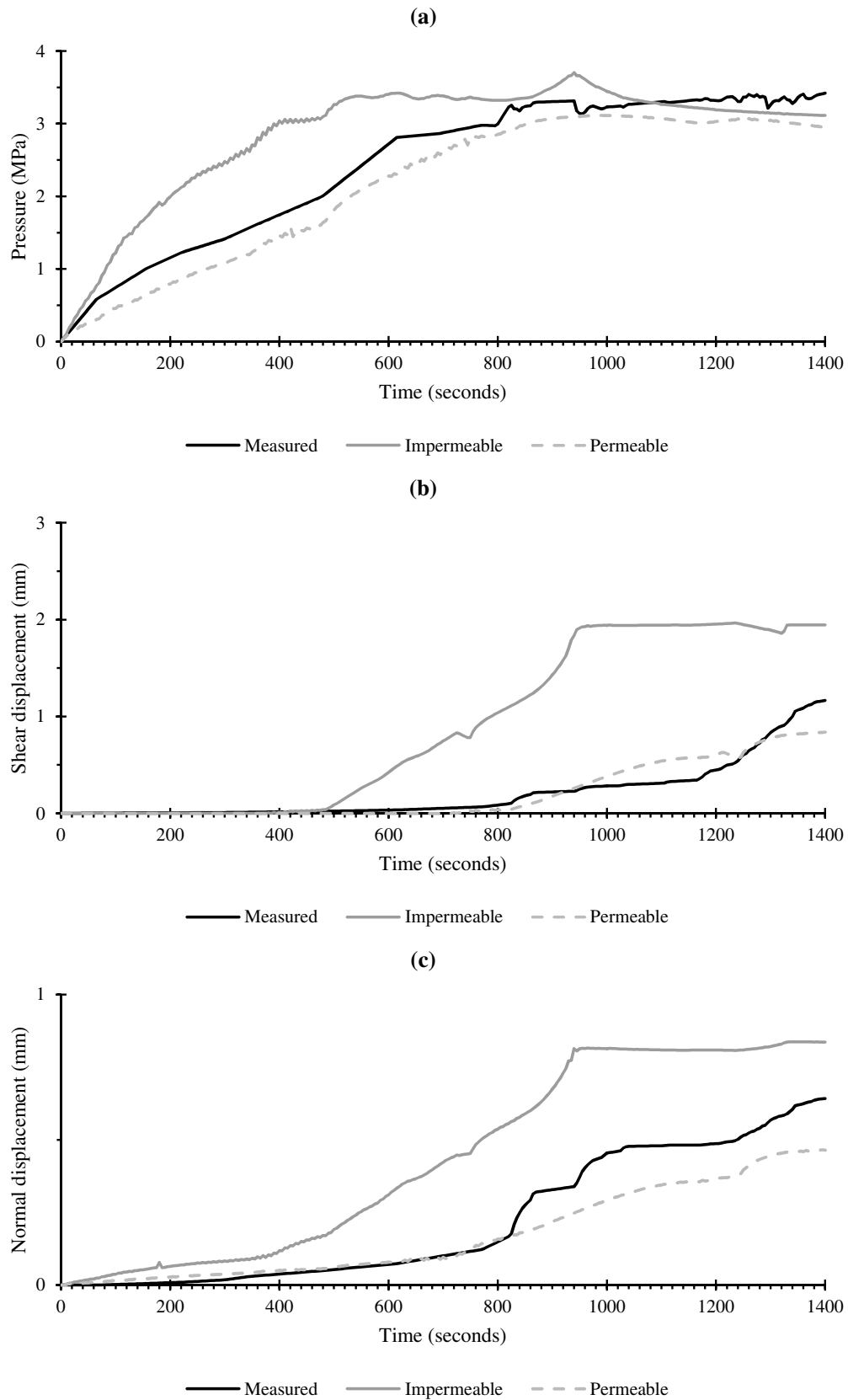


Fig. 13 a Pore pressure, (b) tangential displacement, and (c) normal displacement at the center of the model (injection point) over time for the impermeable and permeable cases using the calibrated values

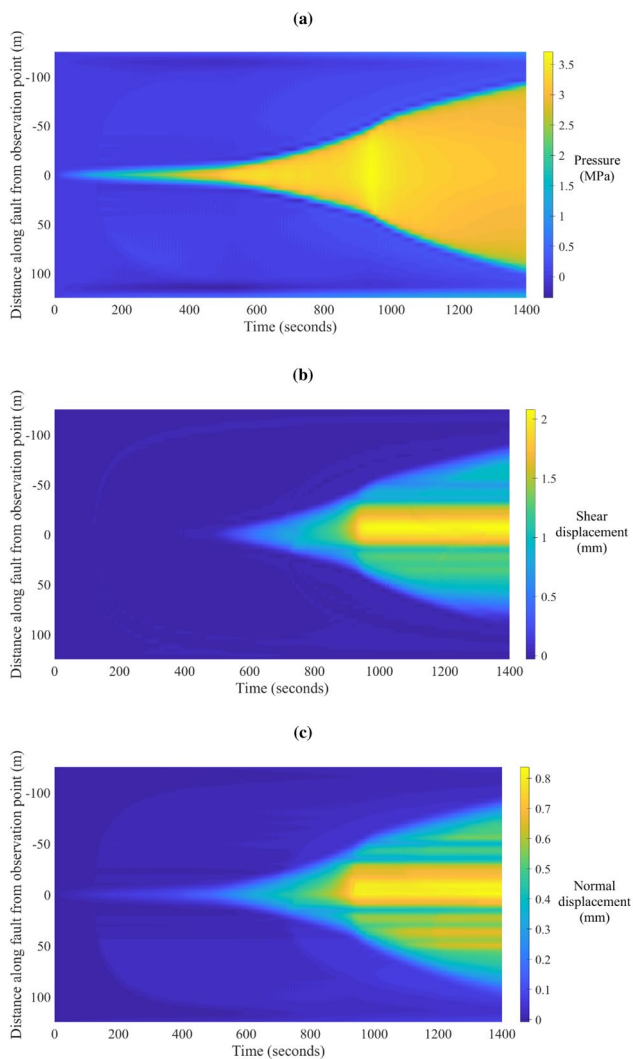


Fig. 14 **a** Pore pressure, **(b)** tangential displacement, and **(c)** normal displacement along the fault over time for the impermeable case using the calibrated values

compared with the permeable case. The non-uniform shear displacements are caused by the center of the fault becoming tensile and increasing the shear stress away from this region. This shear displacement then opens the fault (increases the normal displacement) as a result of dilation. Note that positive values from the injection (observation) point are deeper.

6.2.2 Comparison Between the UDEC and Impermeable X-FEM Models

To illustrate how the impermeable X-FEM model compares to the commercial code UDEC, the calibrated case parameters are used. The impermeable X-FEM model used a constant frictional coefficient to represent more closely the UDEC simulation. Note that the UDEC simulation used approximately 0.0002 s as the time interval, since it uses

an explicit time integration method, whereas the X-FEM model used 5 s, because this uses an implicit time integration scheme. The UDEC model took approximately 55,680 s to complete the analysis, whereas the X-FEM simulation took approximately 16,822 s to finish (about 30% of the UDEC total run time). The comparison of the two results is shown in Fig. 15. In addition, the initial mesh of the UDEC model was chosen to be 50×50 elements, whereas the X-FEM model needed 50×51 elements in the x and y directions, respectively (as discussed previously).

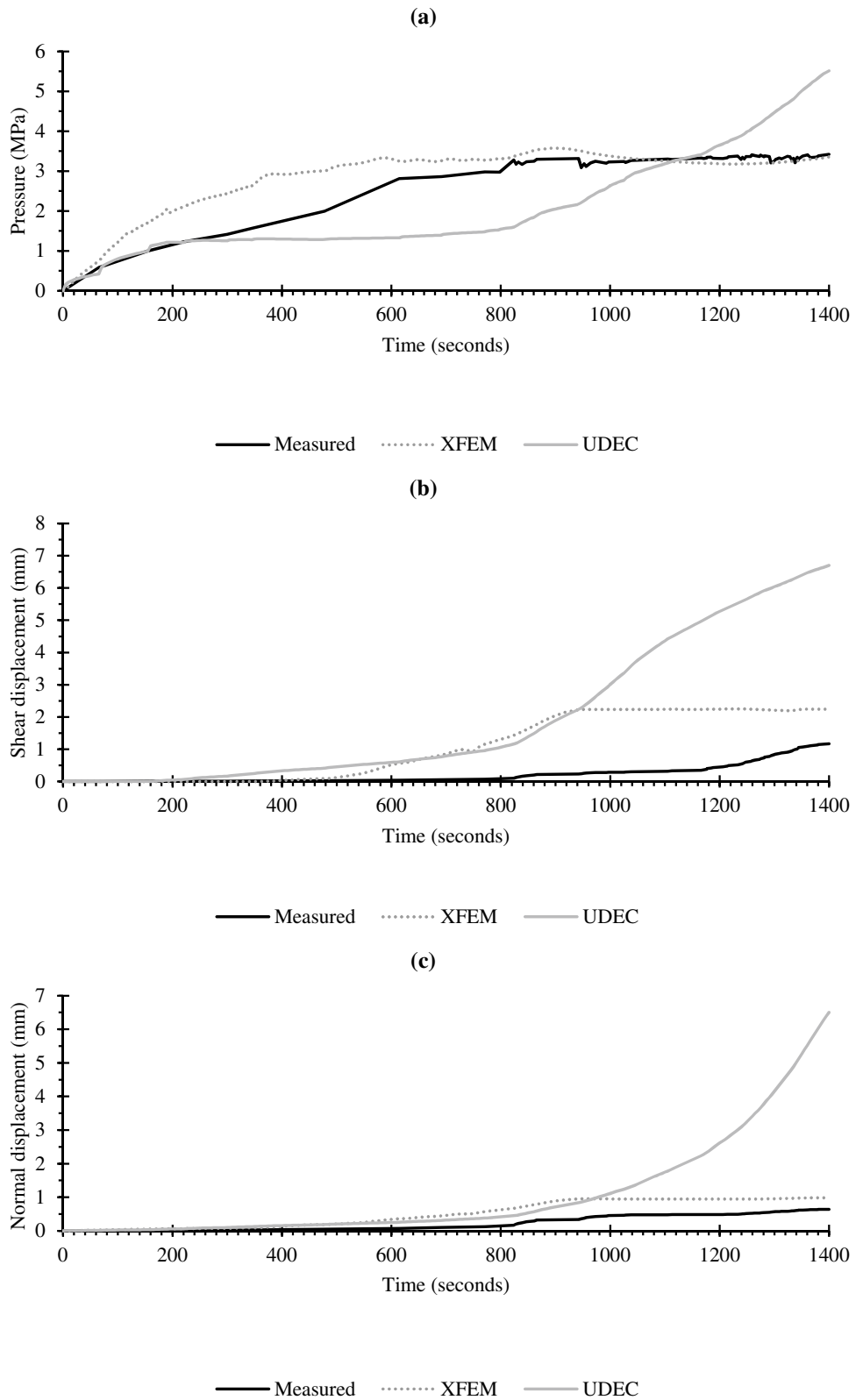
The pore pressures at the injection point for the impermeable X-FEM model were close to the in-situ experimental data, whereas the UDEC fluid pressure increased slowly, then remained nearly constant from approximately 200 s–800 s, before then increasing steadily until the end of the simulation, as shown in Fig. 15a. The shear displacement was greater than the in-situ data in the results from both models, as shown in Fig. 15b. This indicates that fluid exchange between the fault and the rock mass is an important mechanism that modulates the magnitude of shear displacement during the simulations. It is also to be noted that the UDEC simulation produced higher initial slip, compared to the X-FEM model, due to the higher early pore pressure at the injection point, while the X-FEM result matches the measurement during the initial stage of the injection. The UDEC model produces significantly more fault opening earlier in the simulation, before reducing to less than the X-FEM simulation, although increasing rapidly after approximately 940 s when compared with the X-FEM simulation. Figure 16 shows the change in pore pressure and displacements (both shear and normal) along the fault over time for the impermeable X-FEM simulation (using a constant frictional coefficient) and Fig. 17 shows the same data for the impermeable UDEC simulation. Note that the same mechanism is responsible for the non-uniform displacements, i.e., the center of the fault becomes tensile and increases the shear stress away from this region causing more shear displacement and hence normal displacement resulting from dilation.

These simulations indicate that the X-FEM model is more capable of reproducing the data from the in-situ experiment when compared to the UDEC simulation. In addition, the lower computational cost of X-FEM makes it attractive for modelling fault mechanics due to fluid injection.

6.3 Consideration of Additional Physical Phenomena, Geometrical Properties and Parameters

The modelling technique presented in this study uses one through-going strong discontinuity to represent the fault core. It is possible to introduce fault tips into this X-FEM approach and consider fault propagation from fluid injection.

Fig. 15 **(a)** Pore pressure, **(b)** tangential displacement, and **(c)** normal displacement at the center of the model (injection point) over time for the impermeable X-FEM and UDEC models using a constant frictional coefficient (and considering the calibrated parameters)



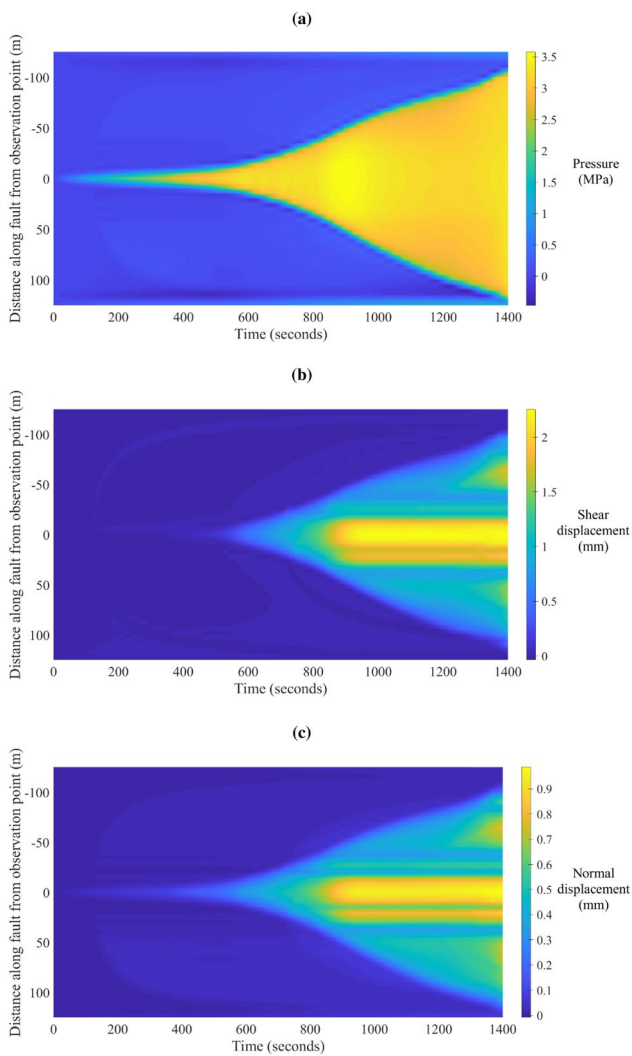


Fig. 16 **a** Pore pressure, **(b)** tangential displacement, and **(c)** normal displacement along the fault over time for the impermeable X-FEM model using a constant frictional coefficient (and considering the calibrated parameters)

Since fault propagation is a complex phenomenon, it was not considered. In addition, because the pressurized zone along the fault is small relatively compared to the length of this fault it is expected that propagation of the fault is unlikely to occur in this case. However, fault propagation is expected to have an influence on the seismicity produced from slipping faults that are smaller than the one in the in-situ experiment that is reproduced via this X-FEM model, or if there is more fluid injection over a longer period of time.

This X-FEM approach assumes quasi-static deformation by neglecting the inertial term, similar to other studies (Vilarrasa et al. 2013; Jha and Juanes 2014). Although this assumption is appropriate for aseismic fault slip, when seismicity occurs the inertial term is no longer negligible (Jha and Juanes 2014).

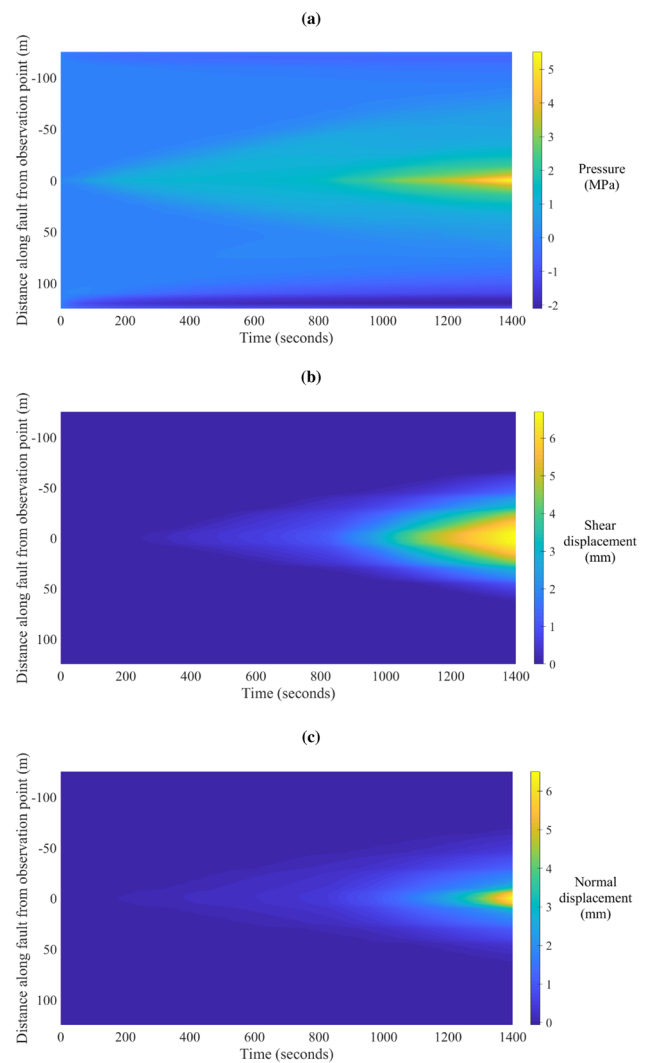


Fig. 17 **a** Pore pressure, **(b)** tangential displacement, and **(c)** normal displacement along the fault over time for the impermeable UDEC model using a constant frictional coefficient (and considering the calibrated parameters)

The presented X-FEM approach has the capability to account for inertial effects and this will be addressed in further studies.

7 Conclusions

This study has outlined the fully coupled (in terms of displacements and pore pressure) X-FEM approach, which made possible modelling of fluid injection at the center of a strong discontinuity that represented a fault. This method accounts for both the fluid flow within the fault and fluid leak off into the rock mass (into the damage zone). The proposed method was compared to the pressure and displacement history recorded in an in-situ experiment. After calibration, using bounds from the literature, the coupled X-FEM approach produced comparable results to the in-situ

experiment. This suggests this X-FEM approach is versatile enough to produce reasonable results. Dynamic analysis should be conducted when the fault slips due to the reduction in compressive effective normal pressure on the fault, which could lead to a means to predict seismicity due to fluid injection. This coupled X-FEM approach could also be extended to three-dimensional analysis.

Funding This work was supported by the Japan Society for the Promotion of Science (JSPS) project number: 19K15493.

Data Availability The datasets generated during and/or analyzed during the current study are available from the corresponding author on reasonable request.

Code Availability The custom code will be made available in the future.

Compliance with Ethical Standards

Conflict of interest The authors declare they have no conflict of interest.

Appendix

Below, the least sensitive parameters are listed in order of the largest change in the weighted objective function to the smallest. In addition, the projected mechanisms influencing response are given for each parameter.

- Base friction coefficient (μ_0)

The higher the base friction coefficient the later the slip occurs in the model as stresses build, which reduces the overall displacement (in both normal and shear directions) at the location of injection (that is, the center of the fault).

- a parameter

The higher the a parameter the less slip occurs on the fault, since this parameter controls the magnitude of the velocity strengthening effect, which in turn, through the base dilation angle, reduces the normal displacement.

- Tangential stiffness (\bar{k}_T)

The higher the tangential stiffness the less movement required to increase the shear stress along the fault. The higher shear stress induces slip and hence produces more displacement (in both shear and normal directions) because of the base value for the dilation angle.

- Kappa factor (κ)

The higher the kappa factor the lower the fault permeability. This causes higher pressures and displacement along the fault.

- Damage zone Poisson's ratio (ν)

The damage zone Poisson's ratio parameter has a similar influence to that of the intact Poisson's ratio. That is, the lower the value the less effect the lateral (along fault) compressive in-situ stress has on the displacement (in both shear and normal directions).

- Biot poroelastic constant (α_{Biot})

The higher the Biot poroelastic constant, the higher the effective stresses in the simulation (where tensile effective stresses are positive, as defined before). The higher (or less compressive) the effective stresses are, the more the displacement. However, since the range in this value obtained from the literature is small, this is one of the least influential parameters on the objective function.

- Density (ρ_s)

The greater the rock mass density the larger the slip induced at the center of the fault. Note that changing density did not alter the result significantly; therefore, this parameter is classified as independent.

References

- Agosta F, Prasad M, Aydin A (2007) Physical properties of carbonate fault rocks, fucino basin (Central Italy): implications for fault seal in platform carbonates. *Geofluids* 7:19–32
- Béchet É, Minnebo H, Moës N, Burgardt B (2005) Improved implementation and robustness study of the X-FEM for stress analysis around cracks. *Int J Numer Methods Eng* 64:1033–1056
- Bell FG (2013) *Engineering properties of soils and rocks*. Elsevier
- Billi A, Salvini F, Storti F (2003) The damage zone-fault core transition in carbonate rocks: implications for fault growth, structure and permeability. *J Struct Geol* 25:1779–1794. [https://doi.org/10.1016/S0191-8141\(03\)00037-3](https://doi.org/10.1016/S0191-8141(03)00037-3)
- Biot MA (1941) General theory of three-dimensional consolidation. *J Appl Phys* 12:155–164
- Brady BHG, Brown ET (2013) *Rock mechanics: for underground mining*. Springer Science & Business Media
- Caine JS, Bruhn RL, Forster CB (2010) Internal structure, fault rocks, and inferences regarding deformation, fluid flow, and mineralization in the seismogenic Stillwater normal fault, Dixie Valley, Nevada. *J Struct Geol* 32:1576–1589
- Cappa F, Guglielmi Y, Rutqvist J et al (2006) Hydromechanical modelling of pulse tests that measure fluid pressure and fracture normal displacement at the Coaraze Laboratory site, France. *Int J Rock Mech Min Sci* 43:1062–1082

- Choi J-H, Edwards P, Ko K, Kim Y-S (2016) Definition and classification of fault damage zones: a review and a new methodological approach. *Earth-Sci Rev* 152:70–87
- Cornet FH, Helm J, Poitrenaud H, Etchecopar A (1997) Seismic and aseismic slips induced by large-scale fluid injections. In: *Pure and Applied Geophysics*. Springer, pp 563–583
- Cundall PA (1980) UDEC-A Generalised Distinct Element Program for Modelling Jointed Rock. Cundall (Peter) Associates Virginia Water (England)
- Cuss RJ, Harrington JF (2016) An experimental study of the potential for fault reactivation during changes in gas and pore-water pressure. *Int J Greenh Gas Control* 53:41–55. <https://doi.org/10.1016/j.ijggc.2016.07.028>
- Da Silva MR, Schroeder C, Verbrugge J-C (2010) Poroelastic behaviour of a water-saturated limestone. *Int J Rock Mech Min Sci* 47:797–807
- Dieterich JH (1979) Modeling of rock friction: 1. Experimental results and constitutive equations. *J Geophys Res Solid Earth* 84:2161–2168
- Doherty JE, Hunt RJ (2010) Approaches to highly parameterized inversion: a guide to using PEST for groundwater-model calibration. US Department of the Interior, US Geological Survey
- Eftekhari M, Baghbanan A, Bagherpour R (2014) The effect of fracture patterns on penetration rate of TBM in fractured rock mass using probabilistic numerical approach. *Arab J Geosci* 7:5321–5331
- Ellsworth WL (2013) Injection-induced earthquakes. *Science* (80-) 341:
- Fan Z, Eichhubl P, Gale JFW (2016) Geomechanical analysis of fluid injection and seismic fault slip for the Mw4. 8 Timpson, Texas, earthquake sequence. *J Geophys Res Solid Earth* 121:2798–2812
- Finsterle S, Zhang Y (2011) Solving iTOUGH2 simulation and optimization problems using the PEST protocol. *Environ Model Softw* 26:959–968. <https://doi.org/10.1016/j.envsoft.2011.02.008>
- Ghassemi A, Tarasovs S, Cheng AH-D (2007) A 3-D study of the effects of thermomechanical loads on fracture slip in enhanced geothermal reservoirs. *Int J Rock Mech Min Sci* 44:1132–1148. <https://doi.org/10.1016/j.ijrmms.2007.07.016>
- Giner E, Sukumar N, Tarancón JE, Fuenmayor FJ (2009) An Abaqus implementation of the extended finite element method. *Eng Fract Mech* 76:347–368. <https://doi.org/10.1016/j.engfractmech.2008.10.015>
- Guerriero V, Mazzoli S, Iannace A et al (2013) A permeability model for naturally fractured carbonate reservoirs. *Mar Pet Geol* 40:115–134. <https://doi.org/10.1016/j.marpetgeo.2012.11.002>
- Guglielmi Y, Cappa F, Amitrano D (2008) High-definition analysis of fluid-induced seismicity related to the mesoscale hydromechanical properties of a fault zone. *Geophys Res Lett* 35:
- Guglielmi Y, Cappa F, Avouac J-P, et al (2015a) Seismicity triggered by fluid injection-induced aseismic slip. *Science* (80-) 348:1224 LP–1226
- Guglielmi Y, Cappa F, Lançon H, et al (2013) ISRM suggested method for step-rate injection method for fracture in-situ properties (SIM-FIP): Using a 3-components borehole deformation sensor. In: *The ISRM Suggested Methods for Rock Characterization, Testing and Monitoring: 2007–2014*. Springer, pp 179–186
- Guglielmi Y, Elsworth D, Cappa F et al (2015) In situ observations on the coupling between hydraulic diffusivity and displacements during fault reactivation in shales. *J Geophys Res Solid Earth* 120:7729–7748
- Itasca Consulting Group (1997) FLAC 3D, Fast Lagrangian Analysis of Continua in 3 Dimensions
- Jha B, Juanes R (2014) Coupled multiphase flow and poromechanics: a computational model of pore pressure effects on fault slip and earthquake triggering. *Water Resour Res* 50:3776–3808
- Khademian Z, Nakagawa M, Ozbay U (2018) Modeling injection-induced seismicity through calculation of radiated seismic energy. *J Nat Gas Sci Eng* 52:582–590. <https://doi.org/10.1016/j.jngse.2018.02.013>
- Khoei AR (2014) *Extended finite element method: theory and applications*. John Wiley & Sons
- Khoei AR, Vahab M, Hirmand M (2018) An enriched-FEM technique for numerical simulation of interacting discontinuities in naturally fractured porous media. *Comput Methods Appl Mech Eng* 331:197–231. <https://doi.org/10.1016/j.cma.2017.11.016>
- Kohl T, Evans KF, Hopkirk RJ, Rybach L (1995) Coupled hydraulic, thermal and mechanical considerations for the simulation of hot dry rock reservoirs. *Geothermics* 24:345–359
- Kohl T, Mégel T (2007) Predictive modeling of reservoir response to hydraulic stimulations at the European EGS site Soultz-sous-Forêts. *Int J Rock Mech Min Sci* 44:1118–1131. <https://doi.org/10.1016/j.ijrmms.2007.07.022>
- Konstantinovskaya E, Rutqvist J, Malo M (2014) CO₂ storage and potential fault instability in the St. Lawrence Lowlands sedimentary basin (Quebec, Canada): insights from coupled reservoir-geomechanical modeling. *Int J Greenh Gas Control* 22:88–110
- Kostakioti A, Xypolias P, Kokkalas S, Doutsos T (2004) Quantitative analysis of deformation along the fault damage zone of the Klimatia thrust (NW Greece, Ionian Zone). *Bull Geol Soc Greece* 36:1643–1651
- Lion M, Skoczylas F, Ledésert B (2004) Determination of the main hydraulic and poro-elastic properties of a limestone from Bourgogne, France. *Int J Rock Mech Min Sci* 41:915–925
- Lion M, Skoczylas F, Ledésert B (2005) Effects of heating on the hydraulic and poroelastic properties of Bourgogne limestone. *Int J Rock Mech Min Sci* 42:508–520
- Lorig LJ, Hobbs BE (1990) Numerical modelling of slip instability using the distinct element method with state variable friction laws. In: *International Journal of Rock Mechanics and Mining Sciences & Geomechanics Abstracts*. Elsevier, pp 525–534
- Majer EL, Baria R, Stark M et al (2007) Induced seismicity associated with enhanced geothermal systems. *Geothermics* 36:185–222. <https://doi.org/10.1016/j.geothermics.2007.03.003>
- Marone C (1998) Laboratory-derived friction laws and their application to seismic faulting. *Annu Rev Earth Planet Sci* 26:643–696
- McGarr A (2014) Maximum magnitude earthquakes induced by fluid injection. *J Geophys Res solid earth* 119:1008–1019
- Meier S, Bauer JF, Philipp SL (2015) Fault zone characteristics, fracture systems and permeability implications of Middle Triassic Muschelkalk in Southwest Germany. *J Struct Geol* 70:170–189
- Micarelli L, Benedicto A, Wibberley CAJ (2006) Structural evolution and permeability of normal fault zones in highly porous carbonate rocks. *J Struct Geol* 28:1214–1227
- Moeck I, Kwiatek G, Zimmermann G (2009) Slip tendency analysis, fault reactivation potential and induced seismicity in a deep geothermal reservoir. *J Struct Geol* 31:1174–1182. <https://doi.org/10.1016/j.jsg.2009.06.012>
- Mohammadnejad T, Khoei AR (2013) An extended finite element method for hydraulic fracture propagation in deformable porous media with the cohesive crack model. *Finite Elem Anal Des* 73:77–95
- Moré JJ (1978) The Levenberg-Marquardt algorithm: implementation and theory. In: *Numerical analysis*. Springer, pp 105–116
- Nagata K, Nakatani M, Yoshida S (2012) A revised rate- and state-dependent friction law obtained by constraining constitutive and evolution laws separately with laboratory data. *J Geophys Res Solid Earth* 117:
- Nicholson C, Wesson RL (1992) Triggered earthquakes and deep well activities. *Pure Appl Geophys* 139:561–578. <https://doi.org/10.1007/BF00879951>

- Niwa M, Mizuochi Y, Tanase A (2009) Reconstructing the evolution of fault zone architecture: field-based study of the core region of the Atera Fault, Central Japan. *Isl Arc* 18:577–598
- Oliver DS, Chen Y (2011) Recent progress on reservoir history matching: a review. *Comput Geosci* 15:185–221. <https://doi.org/10.1007/s10596-010-9194-2>
- Pan P-Z, Rutqvist J, Feng X-T, Yan F (2013) Modeling of caprock discontinuous fracturing during CO₂ injection into a deep brine aquifer. *Int J Greenh Gas Control* 19:559–575. <https://doi.org/10.1016/J.IJGGC.2013.10.016>
- Prévost JH, Sukumar N (2016) Faults simulations for three-dimensional reservoir-geomechanical models with the extended finite element method. *J Mech Phys Solids* 86:1–18. <https://doi.org/10.1016/J.JMPS.2015.09.014>
- Pruess K, Oldenburg CM, Moridis GJ (1999) TOUGH2 user's guide version 2
- Raleigh CB, Healy JH, Bredehoeft JD (1976) An experiment in earthquake control at Rangely, Colorado. *Science* (80-) 191:1230–1237. doi: 10.1126/science.191.4233.1230
- Ran G, Eyal S, Yoseph Y et al (2014) The permeability of fault zones: a case study of the Dead Sea rift (Middle East). *Hydrogeol J* 22:425–440. <https://doi.org/10.1007/s10040-013-1055-3>
- Renshaw CE (1995) On the relationship between mechanical and hydraulic apertures in rough-walled fractures. *J Geophys Res Solid Earth* 100:24629–24636
- Ruina A (1983) Slip instability and state variable friction laws. *J Geophys Res Solid Earth* 88:10359–10370
- Rutqvist J (2015) Fractured rock stress-permeability relationships from in situ data and effects of temperature and chemical-mechanical couplings. *Geofluids* 15:48–66
- Rutqvist J, Birkholzer J, Cappa F, Tsang C-F (2007) Estimating maximum sustainable injection pressure during geological sequestration of CO₂ using coupled fluid flow and geomechanical fault-slip analysis. *Energy Convers Manag* 48:1798–1807. <https://doi.org/10.1016/j.enconman.2007.01.021>
- Rutqvist J, Rinaldi AP, Cappa F, Moridis GJ (2013) Modeling of fault reactivation and induced seismicity during hydraulic fracturing of shale-gas reservoirs. *J Pet Sci Eng* 107:31–44. <https://doi.org/10.1016/J.PETROL.2013.04.023>
- Rutqvist J, Rinaldi AP, Cappa F, Moridis GJ (2015) Modeling of fault activation and seismicity by injection directly into a fault zone associated with hydraulic fracturing of shale-gas reservoirs. *J Pet Sci Eng* 127:377–386. <https://doi.org/10.1016/J.PETROL.2015.01.019>
- Rutqvist J, Wu Y-S, Tsang C-F, Bodvarsson G (2002) A modeling approach for analysis of coupled multiphase fluid flow, heat transfer, and deformation in fractured porous rock. *Int J Rock Mech Min Sci* 39:429–442. [https://doi.org/10.1016/S1365-1609\(02\)00022-9](https://doi.org/10.1016/S1365-1609(02)00022-9)
- Savage HM, Brodsky EE (2011) Collateral damage: Evolution with displacement of fracture distribution and secondary fault strands in fault damage zones. *J Geophys Res Solid Earth* 116:
- Scotti O, Cornet FH (1994) In situ evidence for fluid-induced aseismic slip events along fault zones. In: *International Journal of Rock Mechanics and Mining Sciences and Geomechanics Abstracts*. Oxford; New York: Pergamon Press, 1974-c1996., pp 347–358
- Streit JE, Hillis RR (2004) Estimating fault stability and sustainable fluid pressures for underground storage of CO₂ in porous rock. *Energy* 29:1445–1456. <https://doi.org/10.1016/j.energy.2004.03.078>
- Torabi A, Ellingsen T, Johannessen M, Alaei B, Rotevatn A, Chiarella D (2020) Fault zone architecture and its scaling laws: where does the damage zone start and stop? *Geol Soc Lond Special Publ* 496:99–124
- Vallier B, Magnenet V, Schmittbuhl J, Fond C (2018) THM modeling of hydrothermal circulation at Rittershoffen geothermal site. *France Geotherm Energy* 6:22. <https://doi.org/10.1186/s40517-018-0108-1>
- Vilarrasa V, Carrera J, Olivella S (2013) Hydromechanical characterization of CO₂ injection sites. *Int J Greenh Gas Control* 19:665–677. <https://doi.org/10.1016/J.IJGGC.2012.11.014>
- Wiseall AC, Cuss RJ, Hough E, Kemp SJ (2018) The role of fault gouge properties on fault reactivation during hydraulic stimulation; an experimental study using analogue faults. *J Nat Gas Sci Eng* 59:21–34
- Witherspoon PA, Wang JSY, Iwai K, Gale JE (1980) Validity of cubic law for fluid flow in a deformable rock fracture. *Water Resour Res* 16:1016–1024
- Yoshida H, Horii H (2004) Micromechanics-based continuum model for a jointed rock mass and excavation analyses of a large-scale cavern. *Int J Rock Mech Min Sci* 41:119–145. [https://doi.org/10.1016/S1365-1609\(03\)00080-7](https://doi.org/10.1016/S1365-1609(03)00080-7)
- Zangeneh N, Eberhardt E, Bustin RM (2014) Investigation of the influence of natural fractures and in situ stress on hydraulic fracture propagation using a distinct-element approach. *Can Geotech J* 52:926–946
- Zhang X, Sanderson DJ (1996) Numerical modelling of the effects of fault slip on fluid flow around extensional faults. *J Struct Geol* 18:109–119. [https://doi.org/10.1016/0191-8141\(95\)00086-S](https://doi.org/10.1016/0191-8141(95)00086-S)

Publisher's Note Springer Nature remains neutral with regard to jurisdictional claims in published maps and institutional affiliations.